ABSTRACT

Title of Document:	Morphotropic Phase Boundaries in $Tb_{1-x}Dy_xFe_2$ Alloys
	Richard Bergstrom Jr., Doctor of Philosophy, 2013
Directed By:	Professor Manfred Wuttig, Department of Materials Science and Engineering

Magnetostrictive alloys, materials that change in dimension under an applied magnetic field, are desired candidates for transducers. Unfortunately, common magnetostrictive metals, alloys, and oxides produce such small strains that they are not a viable option. In the early 1960's rare earths were found to possess extraordinary magnetostriction values at cryogenic temperatures. When alloyed with traditional transition metals they form a Laves phase compound of the form AB_2. These Laves phase compounds have shown large magnetostriction values, up to 2500με in $TbFe_2$. A major drawback to using these materials as transducers is their huge magnetocrystalline anisotropy constants, K_1 and K_2. However, it was found that $TbFe_2$ and $DyFe_2$ have opposing signs of K_1 and K_2. A pseudo-binary alloy, $Tb_{1-x}Dy_xFe_2$ (Terfenol-D) TDFx, was formed to decrease the total magnetocrystalline anisotropy. The anisotropy reached a room temperature minimum for TDF73. It is suspected that this minimum of the anisotropy is accompanied by a morphotropic

phase boundary (MPB) at which the crystal structure changes from tetragonal to rhombohedral. Unraveling the nature of the temperature and composition dependence of the magnetic and crystalline properties along this MPB is the primary focus of this thesis.

The structure of the TDF alloys was probed through macroscopic and microscopic techniques. The maximum in the DC magnetization at the transition temperature from tetragonal to rhombohedral broadens as the transition temperature is increased. This is attributed to decreasing anisotropy at increased temperature.

Synchrotron and neutron powder diffraction are utilized to elucidate the microscopic changes in the structure and magnetism. Neutron powder diffraction results were somewhat inconclusive but were sufficient to produce magnetic moments that were invariant, within experimental error, across the transition region. Synchrotron powder diffraction was used to probe the structure at temperatures across the MPB. Reitveld refinement of the structure in TDF65 reveals that large strain gradients exist across the MPBs. This was supplemented by temperature dependent scans of various TDF alloys showing a broadening of the phase transition with increasing temperature which we attribute a widening of the meta-stable [100] and [111] easy directions.

Morphotropic Phase Boundaries in $Tb_{1-x}Dy_xFe_2$ Alloys

By

Richard Bergstrom Jr.

Dissertation submitted to the Faculty of the Graduate School of the
University of Maryland, College Park, in partial fulfillment
of the requirements for the degree of
Doctor of Philosophy
2013

Advisory Committee:
Professor Manfred Wuttig, Chair/Advisor
Professor James Cullen
Professor Robert Briber
Dr. Peter Zavalij
Professor Alison Flatau (Dean's Representative)

Dedication

This work is dedicated to my late grandfather, Howard Victor Bergstrom, who valiantly served this country in the African, Sicilian, and European campaigns while deployed overseas for 34 months during World War II.

Acknowledgements

The journey to this point has been long and it wouldn't have been possible without the help of many people. First, I would like to thank my advisor Professor Manfred Wuttig. His commitment to me through two years of a project that produced minimal results showed character few advisors could match. His suggestion that I take up this new project and the many meetings and discussions we've had along the way have proven invaluable to the completion of this thesis. His door is always open and I've come to appreciate his dedication to science. I owe much of the personal and professional success I've enjoyed as a student at the University of Maryland to his support.

I would also like to thank Professor James Cullen for teaching me the basic science surrounding Terfenol alloys as well as the fundamental principles of magnetism. He has proven to be a valuable member of the team and has had many great suggestions for data analysis. Professor Briber was actively involved with my first project and I would like to thank him for his gracious offer to serve on my committee for this new project. This thesis wouldn't have been possible without the assistance of Dr. Zavalij. He spent many hours teaching me Rietveld refinement and offered advice and assistance with my refinements throughout the course of this project. Finally, I would like to thank Professor Flatau for being the dean's representative for my committee. She has been generous enough to let me use several instruments in her laboratory throughout my tenure as a graduate student.

Outside of my committee I would like to thank Dr. Mark Laver who has been a tremendous help in refining the neutron diffraction data and editing my paper. His

persistence in asking the hard questions about our analysis proved invaluable in getting our paper accepted. My groupmates, Yueying Liu, Yemei Han, and Tong Ren, have been a great help throughout my studies. They have been generous enough to take data for me while I was on travel and whatever else I have asked of them and I greatly appreciate it. Outside of my research group I would like to thank Xin Zhang who has been a great source of technical knowledge, Tyler Drye who encapsulated the Terfenol-D samples, and Kevin Kirshenbaum who taught me how to write in LaTeX and assisted with various other minor projects.

I would also like to take the time to thank the members of my family and my future wife. My parents, Frances and Richard Bergstrom, have been there for me through every challenge my life has had. Without their unwavering support both emotionally and financially this document wouldn't be possible. To Brent, I've had many great experiences with you in my lifetime and I would like to thank you for the countless favors you have done for me throughout the years. To Lisa, we were once the closest brother and sister. I have such a deep respect for you and while I'm sorry that we've moved apart I'm glad that you found Tim and the two of you started a family together. Finally to my amazing fiancée, Marilyn Alvarado, I've put you through a stressful two years and I want to thank you for standing by me through the end of my graduate studies. I look forward to what we will accomplish together.

Table of Contents

List of Tables

List of Figures

Chapter 1: Introduction

This dissertation is an attempt to uncover the structure of $Tb_{1-x}Dy_xFe_2$, TDFx, alloys at the Morphotropic Phase Boundary (MPB). These alloys, also known by the trade name Terfenol-D, have the highest magnetostriction of any material at room temperature (1). TDF alloys are thus used in actuators and transducers for commercial applications (2).

TDF is a pseudo binary alloy of $TbFe_2$ and $DyFe_2$ both of which crystallize into the C15 Laves phase. Binary alloys of elements of the same structure tend to form solid solutions e.g. CuNi (3). It follows that pseudo-binary alloys of the perovskites e.g. PZT (4) and the Laves phases e.g. $Tb_{1-x}Dy_xFe_2$ (5), even though slightly more complicated, will also form solid solutions. The distinction of these solid solutions is that the component phases possess ferroic distortions of different symmetry (rhombohedral and tetragonal) below their Curie Temperatures, T_C. These distortions force a transition region between the two phases to form in the composition temperature phase diagram. This region is located at temperatures too low for diffusion. Therefore, a diffusionless strain boundary forms between the phases, the MPB.

The MPB is very important in ferroelectric materials and thus has been studied in great detail (4; 6; 7; 8). MPBs have only recently been reported in ferromagnets (9) and little has been reported on their existence in ferroelastics except the softening of the lattice constants in the Ti-Ni-Fe system (10). Ferroelectrics have a rigid structure that is elastically controlled and thus not expected to vary with temperature. Ferromagnets, however, have spin structures that are governed by a competition between the anisotropy and exchange energies with the former highly temperature dependent. Therefore,

attempts will be made to distinguish the characteristics of TDF alloys at the MPB compared from those of ferroelectrics since in the case of ferromagnets the ferroic order and local atomic displacements can be separated. The MPB region in ferromagnets should also be highly dependent on temperature since the anisotropy energy is temperature dependent.

This chapter will provide a brief phenomenological overview of ferroics. Distinctions will be made between single phase and multiphase ferroics. A brief introduction into ferroelectrics as well as ferroelastics is provided to elucidate parallels that will be drawn upon later. Following this a more detailed introduction will be given to ferromagnets including details of various ferromagnetic characteristics vital to understanding the work performed in this thesis. The morphotropic phase boundary (MPB) is introduced in detail for ferroelectric systems and some older and recent research detailing transition regions and MPBs in ferromagnetic systems is described. We then take a look at the microstructure at the MPB including a description of adaptive martensites and how they can be applied to ferroelectric materials. Finally, magnetostriction is introduced since it is the cornerstone of the interest in Terfenol-D. An overview of magnetostrictive materials is given highlighting the reasons behind the interest in Terfenol-D.

1.1   Ferroic Materials

Ferroic solid state materials are those in which the magnetization, polarization, or strain are spontaneously ordered. We distinguish between singly ferroic, where only one order parameter is ordered, and multiferroic materials, in which more than one of the

ferroic parameters is ordered. Many ferroic parameters exhibit general tendencies that can be analogous to other types of ferroics. In this thesis we deal primarily with ferromagnetic materials but will begin with a brief phenomenological overview of the order/disorder transition characteristics of all singly ordered ferroics to take advantage of the analogous properties of transitions in all ferroics (11).

1.2   Types of Ferroic Materials

Ferroic materials are ordered up to a critical order/disorder transition temperature, which is called the Curie temperature, T_C, for ferromagnetic and ferroelectric materials and the martensite transition temperature for strain ordered ferroics, more commonly called martensites or ferroelastics. At this temperature ferroics undergo a phase change from a high temperature cubic para-phase to a low temperature ferroic phase of lower symmetry (tetragonal, rhombohedral, orthorhombic, etc.). In this transition region they exhibit a large change in physical properties over a small temperature range and are thus interesting for smart materials. While the deviation from cubic symmetry is small, on the order of a few parts per million, the lowering of symmetry alone is sufficient to create technologically useful physical properties.

Materials with more than one type of ferroic distortion, or multiple order parameters, are known as multiferroics. There are two types of multiferroics and each has drawbacks. The first type is the single phase multiferroic, such as the magnetoelectric $YMnO_3$. These materials possess a separate T_C for ferroelectricity and T_N for antiferromagnetism. Unfortunately, these transition temperatures are usually cryogenic limiting device possibilities (12). The notable exceptions to this are the z type ferrites

3

(13) and especially BiFeO3 which has both T_N and T_C well above room temperature. A recent revival of research in $BiFeO_3$ started with a new method of growing thin films (14). The second type of multiferroic is the composite multiferroic, i.e. a ferroelectric/ferromagnetic heterostructure. Since these materials are composites the ferroics can be chosen with tailored T_C's for a specific application (15; 16).

1.2.1   Ferroelectrics

Ferroelectrics are a group of dielectric materials that possess a spontaneous polarization below their ferroelectric Curie temperature, T_C. This spontaneous polarization is the result of symmetry breaking in the unit cell forming a dipole moment produced by the cell distortion. When a ferroelectric is heated through T_C the dielectric constant displays a sharp maximum as shown in Figure 1.1. This maximum of the dielectric constant is of technological importance in designing capacitors since capacitance is proportional to the dielectric constant. At T_C the ferroelectric transitions into a paraelectric phase where cubic symmetry is restored and the dielectric constant quickly decreases from it's peak value (17).
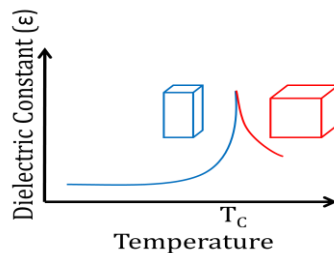
Figure 1.1: Dielectric constant of a ferroelectric near T_C. The dielectric constant reaches a maximum in a narrow temperature window around T_C.

4

Below T_C ferroelectrics can be polarized and reach a maximum polarization known as the saturation polarization, denoted P_S, provided the coercive force is sufficiently small. After reheating above T_C the spontaneous polarization is reduced to zero. Below T_C, ferroelectrics display a nonlinear characteristic in the polarization when applying an electric field loop known as a hysteresis. Within certain symmetry groups, 1, 2, m, 222, mm2, 4, $\bar{4}$, 422, 4 mm, $\bar{4}$2m, 3, 32, 3m, 6, $\bar{6}$, 622, 6 mm, $\bar{6}$2m, 23, $\bar{4}$3m, of dielectrics that include certain ferroelectrics an applied voltage produces an accompanying change of the sample's dimensions due to lattice distortion known as the piezoelectric effect. The process is reversible and the inverse is also true; an applied force causes a change of the polarization/voltage. Electrostriction, which is a property of all dielectrics, also produces a change in the sample dimensions but is generally a non-reversible effect.

Single phase ferroelectrics show a sharp peak in the dielectric constant around T_C (Fig 1.1) which restricts the usefulness of a capacitor made of these ferroelectrics to a narrow temperature window. Multiphase ferroelectrics, like PZNT in which an alloy is formed with different ions that occupy crystallographically equivalent sites, display a diffuse phase transformation. This diffuse phase transformation is a result of slightly different T_C's for each ion which broadens the temperature range of the phase transition (18) as shown in Figure 1.2.
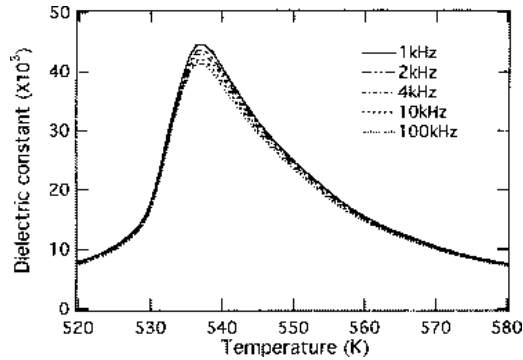
Figure 1.2: Dielectric constant of PZNT with varying temperature and frequency. The peak of the dielectric constant is broadened in this system from substitutional atoms occupying crystallographic equivalent sites with slightly different Curie temperatures **(18)**.

Multiphase ferroelectrics, such as $PbZr_xTi_{1-x}O_3$ (PZT), PZNT, and BCT-BZT, are the most widely used ferroelectric materials. PZT can be made hard or soft by doping with an acceptor (hard) or a donor (soft). The acceptor dopants in hard PZT form oxygen vacancies. These oxygen vacancies reduce the piezoelectric effect but decrease the frictional losses in hard PZT making it useful for actuators. Soft PZT is made by donor doping that creates metal cation vacancies. Soft PZT possesses a high piezoelectric effect and is more suited for transducer applications. Ferroelectric phase diagrams can become quite complicated such as that of PZT, Figure 1.3, where there are several low temperature phases including a rhombohedral, tetragonal, and antiferroelectric. The properties of the ferroelectric can change dramatically along the order-order phase boundaries which are exploited for use in technological applications.

To date most industrial applications use ferroelectrics containing Pb. Due to its harmful effects Pb is already banned in the European Union and poised to be banned in the US. Therefore, it has become necessary to produce Pb free ferroelectrics. Researchers were quick to find systems similar to PZT where one component displays rhombohedral

6

distortion and the other tetragonal to take advantage of the enhanced properties at the MPB (8). These properties will be discussed in greater detail in section 1.2.
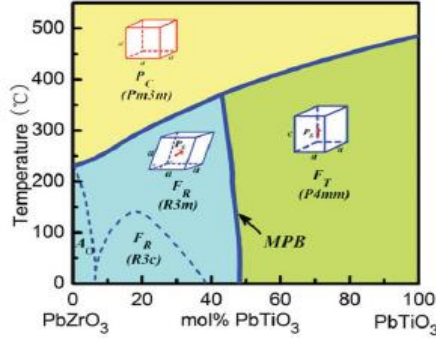
Figure 1.3: Phase diagram of PZT showing a high temperature cubic phase and two major low temperature phases. Rhombohedral symmetry is observed on the $PbZrO_3$ side while tetragonal symmetry is observed on the $PbTiO_3$ side. The MPB is located

1.2.2 Ferromagnets

Ferromagnets, materials that exhibit spontaneous, symmetry breaking, magnetic ordering below a critical temperature T_c (16), are the oldest known ferroic materials. They were originally found in the form of magnetite (Fe_3O_4). A brief overview of the characteristics of ferromagnetic materials follows. For a more detailed review the reader is referred to one of the many texts on the subject, notably (19).

Ferromagnets can be broken into three categories based upon the exchange interaction energy defined by Heisenberg as

$$w_{ij} = -2JS_i \cdot S_j, \tag{1.1}$$

where atoms have spins S_i and S_j and J is the exchange integral (20). The exchange energy is short range and the system will align parallel or antiparallel based on the sign of the exchange integral. If J is positive spins will orient parallel and form a ferromagnet while if J is negative spins align antiparallel and form an antiferromagnet.

7

Ferromagnets are characterized by positive exchange coupling and form domains of parallel aligned moments. Upon applying a sufficiently large magnetic field a point is reached where all moments are aligned and the magnetization can no longer be increased, known as the saturation magnetization (M_S). Ferromagnets usually exhibit hysteresis, Figure 1.4, in the magnetization when cycling the magnetic field that leads to several interesting properties. The hysteresis implies that ferromagnets have a remnant magnetization (M_r), the magnetization remaining when the applied field is removed, and it also implies that ferromagnets possess a nonzero coercive field (H_C), the field required to return the magnetization to zero. Upon heating to the critical temperature, T_C, known as the Curie temperature, ferromagnets transform into a paramagnetic state where thermal energy prevents the spins from aligning thereby eliminating the spontaneous magnetization.
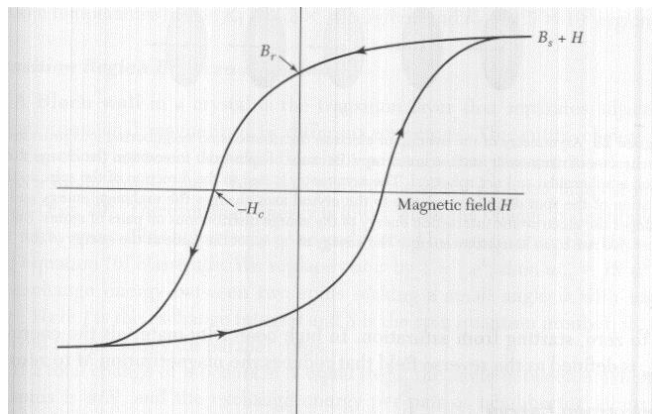
Figure 1.4: Magnetization of a ferromagnet as a function of applied magnetic field. Labeled properties are the saturation magnetization (BS or MS), the remnant magnetization (BR or MR), and the coercive field (HC).

The exchange energy dictates if a material becomes ferromagnetic or antiferromagnetic, however, it doesn't specify a magnetic easy direction, the preferred crystallographic direction of magnetic alignment. In order to determine the easy direction

8

of magnetization one must consider a second energy, the magnetocrystalline anisotropy energy, which for cubic crystals is described by the equation

$$E_K = K_1(\alpha_1^2\alpha_2^2 + \alpha_1^2\alpha_3^2 + \alpha_2^2\alpha_3^2) + K_2(\alpha_1^2\alpha_2^2\alpha_3^2), \qquad (1.2)$$

where α_1, a_2, and α_3 are the directional cosines of the magnetization and K_1 and K_2 are the cubic anisotropy constants. Magnetization can have an easy axis along the [100], [110], or [111] direction depending on the signs of K_1 and K_2 and their ratio. Ferromagnets spontaneously orient along the easy axis but can be rotated away from the easy axis by an applied field, Figure 1.5. As we can see from the figure the magnetization saturates very quickly when applying a field along the easy direction. When applying a field along the hard axis the field required to saturate the ferromagnet is much greater since the moments will first align along the nearest easy direction and then must be rotated from the easy direction requiring a large amount of energy.
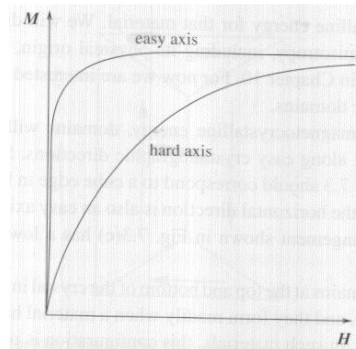
Fig 1.5: Magnetization as a function of applied field of a ferromagnet along its easy and hard crystalline axis (67).

Unlike the exchange energy the anisotropy energy is temperature dependent. It is a function of the interaction between the spontaneous magnetization and the crystal lattice. This implies that at T_C, where the spontaneous magnetization of a ferromagnetic

material vanishes, the magnetocrystalline anisotropy will vanish. Average anisotropy can be calculated by the equation

$$E_a(T) = K_1(0)\langle \beta_1^2\beta_2^2 + \beta_2^2\beta_3^2 + \beta_1^2\beta_3^2 \rangle, \tag{1.3}$$

where β_1, β_2, and β_3 represent the directional cosines of the local spin cluster at a given temperature, $\langle \rangle$ represents the average angular function of the spin clusters, and $K_1(0)$ is the anisotropy at 0K. Written in terms of the reduced magnetization m(T)=M(T)/M(0) we have

$$\langle K^{(n)} \rangle = m(T)^{\frac{n(n+1)}{2}}, \tag{1.4}$$

where n is the nth power angular function which n=2 for uniaxial anisotropy and n=4 for cubic anisotropy.

Antiferromagnets exhibit negative exchange coupling between neighboring magnetic ions indicating they form an anti-parallel spontaneous alignment of magnetic moments. Antiferromagnets display no net spontaneous magnetization below the critical temperature, T_N, known as the Néel temperature, because of anti-parallel moments of equal magnitude. Like ferromagnets, antiferromagnets are paramagnetic above T_N. Anti-parallel spin ordering was first experimentally observed by Shull et al. (21) while performing neutron diffraction studies of MnO above and below T_N. At temperatures below T_N the magnetic lattice constant becomes double the lattice constant above T_N indicating that the repeat distance between like spins equals two unit cells.

Ferrimagnets exhibit negative exchange coupling similar to antiferromagnets. They contain multiple magnetic ions per unit cell with a negative exchange coupling forming an anti-parallel alignment of moments of different magnitude thereby retaining a net spontaneous magnetization Ferrimagnets have minimal hysteresis since the moments

of neighboring ions align anti-parallel. They tend to reach saturation under an applied magnetic field similar to ferromagnets. TDF alloys are ferrimagnets with a positive Fe-Fe and RE-RE exchange ordering the Fe and RE sublattices ferromagnetically and a negative Fe-RE exchange ordering these two sublattices antiferromagnetically with respect to each other.

1.2.3   Ferroelastics

In 1951 a group led by T. Read discovered AuCd alloys that exhibited a martensitic shape-shape transformation upon heating to its high temperature phase (austenite) (22). This effect was later found in many other materials most famously in NiTi by Buehler et al (22). These materials have come to be known as shape memory alloys. When stressed in the low temperature phase (martensite) deformation induced twins remain in the material after the applied stress is relieved leading to a spontaneous strain, similar to the remnant polarization in ferroelectrics or the remnant magnetization in ferromagnets. Upon heating through the austenite phase the twins, which are transformation as well as deformation twins, are removed and the material regains its initial shape, thus titled the "Shape Memory Effect." The inverse elastic susceptibility, the strain induced by an applied stress often referred to as the elastic modulus, is non-linear in these materials because of stress induced martensite. This leads to a property known as superelasticity where stresses past a critical point exhibit a highly nonlinear strain, up to 18% in certain materials (22). This property is displayed when martensite twins begin to form as the material accommodates the stress. The compliance, the inverse of the elastic modulus, of these materials reaches a maximum at the

martensite transition temperature, similar to the dielectric constant of ferroelectrics and the susceptibility of ferromagnets at T_C.

1.3   Morphotropic Phase Boundaries

It was found that the electromechanical properties in ferroelectrics could be greatly enhanced by alloying a ferroelectric with tetragonal symmetry, one whose spontaneous polarization, P_S, is directed parallel to the [100] direction, with a ferroelectric with rhombohedral symmetry, one whose P_S is directed parallel to the [111] direction. When these two different ferroic symmetries are alloyed there must be a region in the composition temperature phase diagram where the rhombohedral phase transitions into the tetragonal phase. The temperature of this transition, $T_{MPB} \ll T_C < T_M$ is $\approx 0.2 T_M$ indicating that diffusion cannot accommodate the stress between the phases. Instead, a special diffusionless strain boundary, the MPB, arises between the two phases. This creates a rich phase diagram where electromechanical properties are at a local maximum when MPBs are present since the material transitions through a low symmetry monoclinic like phase (6; 7; 23) Figure 1.3. Consequently MPBs have been widely studied in ferroelectric materials for several decades (4; 6; 7; 8; 23; 24). Ferroelectrics have nearly infinite anisotropy since the induced polarization is a direct consequence of the lattice distortion. This structural rigidity leads to a direct relationship between the fraction of nanodomains in each orientation and the polarization (25).

MPBs are a generic property of all ferroics that are alloys of multiple constituents with different low temperature symmetries. In ferroelastics MPB like properties were first reported in NiTi where the B19' phase with pseudo tetragonal symmetry transitions into the R-phase with rhombohedral symmetry when a small amount of TiFe is added, Figure 1.6 (left) (10). The compliance increases dramatically when the MPB is approached Figure 1.6 (right).
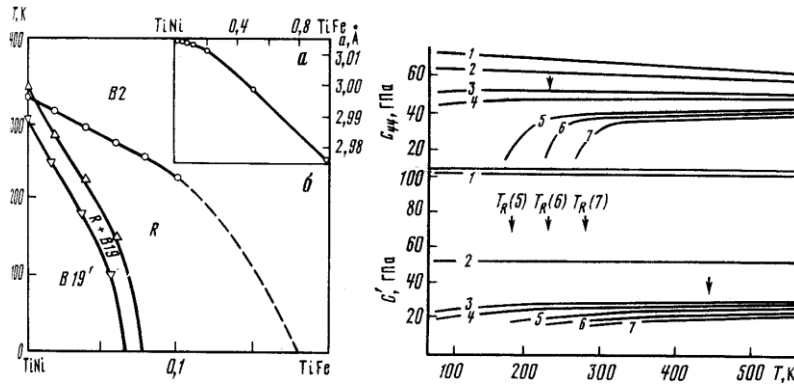
Figure 1.6: (Left) Phase diagram and (Right) elastic constants of TiFe doped TiNi showing high compliance in lines 5, 6, and 7 of the elastic constants. The softening of the elastic constants happens at the MPB between the R phase and the B 19' phase **(10)**.

MPBs have been found in ferroelectrics and ferroelastics so it follows naturally that MPBs can be exploited to enhance the magnetoelastic properties of ferromagnets. The main issue with finding MPBs in ferromagnets centers around the lack of ferromagnetic materials that possess rhombohedral distortion. Only several are known to the author at this time and all of those contain expensive rare earth elements.

Some of the earliest work on ferromagnetic MPBs was performed by Atzmony (26). At the time the suspected mechanism of the [100] to [111] re-orientation was the gradual shift of spins from the [100] to the [111] direction. With this in mind Atzmony performed Mössbauer spectroscopy of Fe^{57} on $Tb_{1-x}Dy_xFe_2$ and other binary and ternary

rare earth iron compounds of the form RFe_2 or $R^1_x R^2_{1-x} Fe_2$. Mössbauer spectra for Fe^{57} have six absorption peaks from the six transitions allowed between the ground state and the excited state (19). The symmetry between the four Fe atoms located in the octahedral sites was observed from the superposition of six line spectra. If the easy axis was pointed along the [100] direction the sites would all be symmetric and the spectrum would be a simple six line type, a [111] type easy axis of magnetization would contain one Fe site different from the other three and thus produce two superimposed six line spectra with a population of 3:1, and a [110] type easy axis would contain two distinct sets of equivalent Fe sites and produce two superimposed six line spectra with a ratio of 2:2. By investigating the Mössbauer spectra at different concentrations and temperatures the directions of the easy axis of magnetization could be plotted in a composition temperature phase diagram. The resultant diagram showing a broad region of spin transition at low temperature and a much narrower region at high temperature, displayed in Figure 1.7.
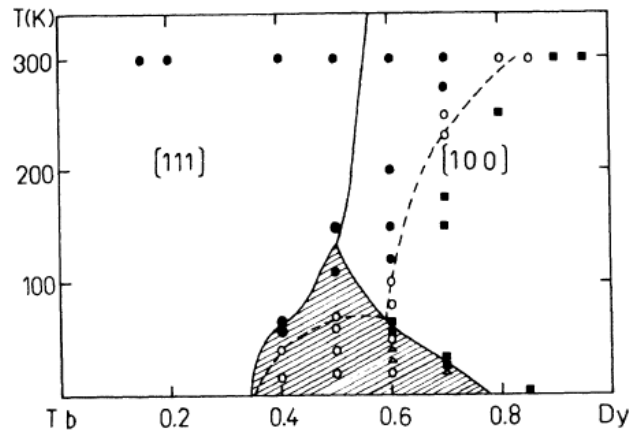
Figure 1.7: Spin orientation diagram of TDF constructed from Fe^{57} Mossbauer spectroscopy. The dashed lines indicate the transition from the low temperature [100] oriented spins to the high temperature [111] oriented spins (26).

14

While these early reports focused on spin reorientation the focus has now shifted to finding MPBs in ferromagnets. Yang et al. (9) have recently reported on a MPB in the $TbCo_2$-$DyCo_2$ system. Their high resolution synchrotron diffraction patterns show peak splitting in the 222 diffraction peak of $Tb_{30}Dy_{70}Co_2$ at 150K indicating a rhombohedral distortion and in the 800 diffraction peak at 90K indicating a tetragonal distortion and at 110K simultaneous 800 and 222 peak splitting indicating the coexistence of both phases, Figure 1.8. The coexistence of both phases indicates that the transition from tetragonal to rhombohedral distortion is a first order phase transformation. This work was the first to point out that the boundary between the rhombohedral and tetragonal phases is magnetoelastic and that the accompanying phase transition is of first order. The temperature region where MPBs exist is accompanied by a peak in the magnetic susceptibility and magnetostrictive figure of merit as well as a minimum in the coercive field. Unfortunately, T_C in the $TbCo_2$-$DyCo_2$ system is cryogenic so its uses remain limited.
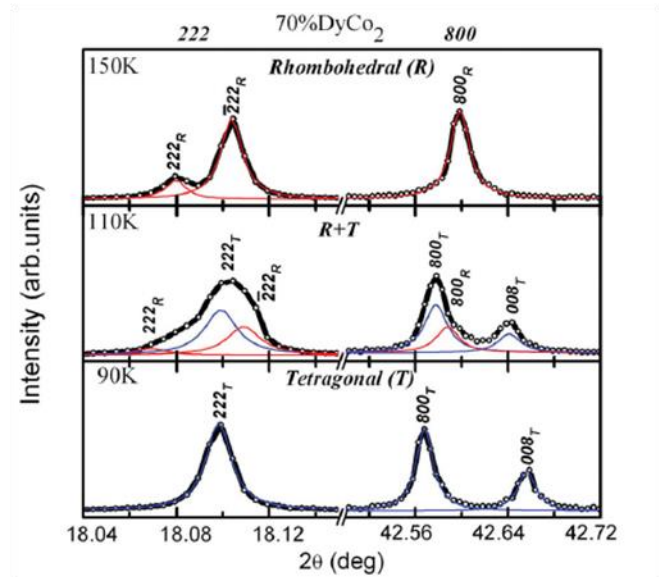
Figure 1.8: In situ synchrotron diffraction data of $Tb_{30}Dy_{70}Co_2$ where peak splitting in the 800 peak is observed at 90K, splitting in the 222 peak is observed at 150K, and splitting in both the 800 and 222 peaks is observed at 110K **(9)**.

Ferromagnets are analogous to ferroelectrics with the slight distinction that the polarization in a ferroelectric is a direct consequence of the local atomic displacement in the lattice, whereas the magnetic moment created in a ferromagnet is the result of spin orbit coupling changes due to ion displacement (11). In the case of ferroelectrics the structure is rigid and the polarization is controlled by elastic interactions. Therefore, the polarization can be summed as a mixture of the variants producing polarizations in the [100] and [111] directions (25). In ferromagnets the magnetization direction is not similarly rigid it can relax as it constitutes a compromise of the exchange and anisotropy energies. It thus becomes necessary to examine the microstructural properties in the MPB regions.

16

1.3.1 Microstructure at the Morphotropic Phase Boundary

Lower symmetry phases were first reported in PZT and PZNT near the MPB in 1999 (23; 27) by Noheda. Two competing models to describe the microstructure have been forwarded. In the first model, presented by Noheda himself, supercells with local monoclinic distortions explain the additional peak splitting. The second theory, developed by Khatchaturyan and coworkers, argues that since intrinsic relations between the lattice parameters exist the phase must be made up of nanodomains formed from orientational variants of the parent phases which exhibit a compound monoclinic symmetry when probed by diffraction (6; 28; 29).

To gain insight into the nanotwin theory we start with an example of two orthogonal variants of a tetragonal ferroelectric. It will be shown that under diffraction this structure looks orthorhombic.

When considering phase diagrams such as PtPd there is a high temperature liquid phase and a low temperature solid solution. Below the solidus line we can see that there is no need to have a second phase form to accommodate the FCC phase from Pt or Pd because they are isomorphous and can readily be exchanged in the lattice through diffusion as T_M is quite large. In the case of PZT where a second phase transition takes place at much at much lower temperatures $T_c \sim \frac{T_M}{7}$ there is little thermal energy available for diffusion to facilitate the phase transition so a diffusionless transformation is needed to adapt the two non-isomorphous low temperature phases. In the case of two tetragonal variants Figure 1.9 (a) we can see that one twin is slightly longer and the other is slightly taller. Since these are nanodomains they are much smaller than the coherence length of the X-ray beam. Therefore, when performing diffraction on a large number of these

domains we would find that on average the structure is monoclinic (6), however, the monoclinic angle, β, is negligible so for the mathematical treatment we will neglect it and assume an orthorhombic structure. Illustrated below is a diagram of the two structures fitted together Figure 1.9 (b-c).
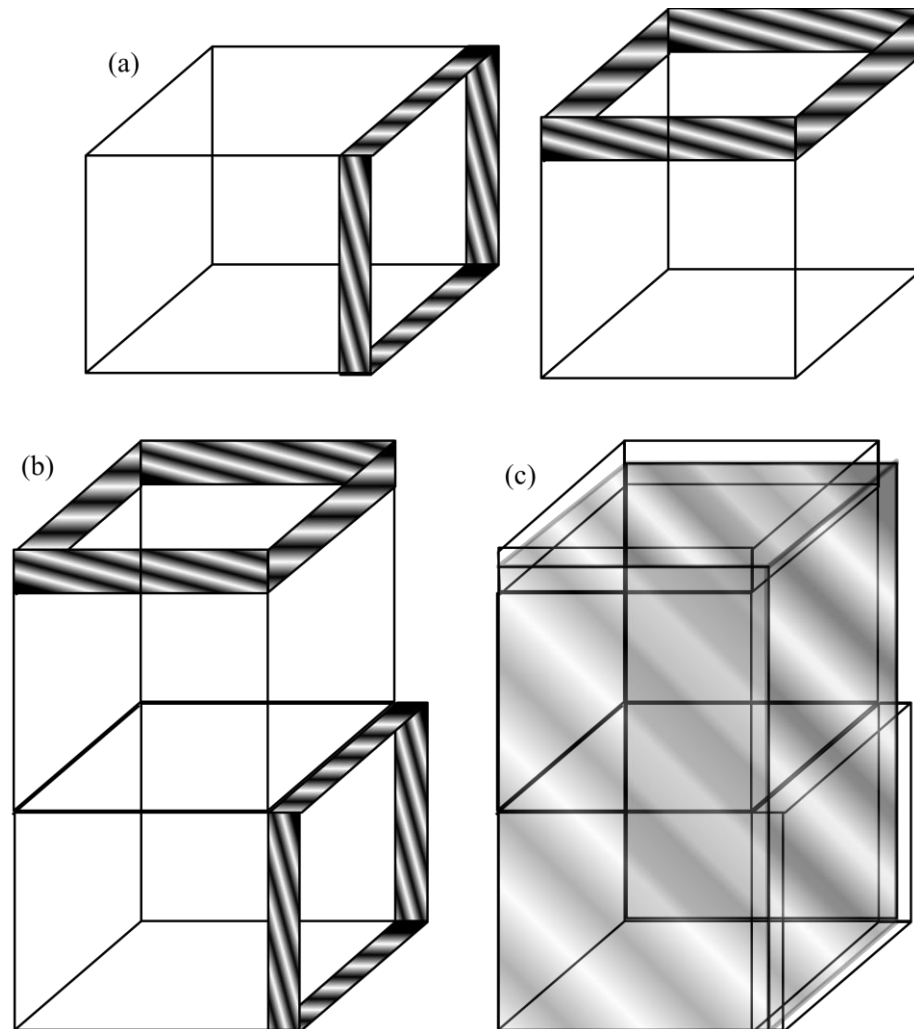
Fig 1.9: (a) Two tetragonal nanodomain variants. (b) Composite sketch of the two tetragonal nanodomains. (c) Average orthorhombic (a≠b≠c) structure of the two nanodomains as seen by a diffracting beam.

The model developed to describe this new form of twinning was based on earlier work in meso-phases called an adaptive martensite (30). A simple transition from cubic to tetragonal causes large internal energy and strain energy so an intermediary adaptive

18

phase is necessary. When decreasing temperature martensites transition through a low symmetry adaptive meso-phase between the parent and the martensite phase. The transition through this phase accommodates the nucleation of the low temperature phase since the adaptive phase minimizes elastic energy. The adaptive phase features a nanotwinned lattice to minimize the elastic misfit energy between the high and low temperature phases. The size of λ, the periodicity of martensite, is given by

$$\lambda \sim \sqrt{\frac{\gamma_{tw}}{\mu \epsilon_0^2}} D, \tag{1.5}$$

where D is the mesoscale dimension of the martensite nucleus, γ_{tw} is the twin surface energy, $\mu \epsilon_0^2$ is the elastic energy. Considering the situation where the mesoscale dimension and twin surface energy are small and the elastic energy is large the twin size conformally decreases constrained by the fixed ratio of the volume fraction, ω (30). This adaptive lattice shares one lattice parameter with the parent cubic phase and one lattice parameter with the martensite to form a pseudo orthorhombic structure,

$$a_{ad} = a_c$$

$$b_{ad} = a_t + c_t - a_c$$

$$c_{ad} = a_t \tag{1.6}$$

where a_{ad}, b_{ad}, and c_{ad} are the adaptive martensite lattice parameters, a_c is the parent cubic lattice parameter, and a_t, and c_t are the tetragonal martensite lattice parameters. This allows a smooth transition between phases as the misfit energy is minimized. The experimentally observed lattice constants of the FePd system are shown in Figure 1.10 along with the calculated lattice constants from the adaptive theory.
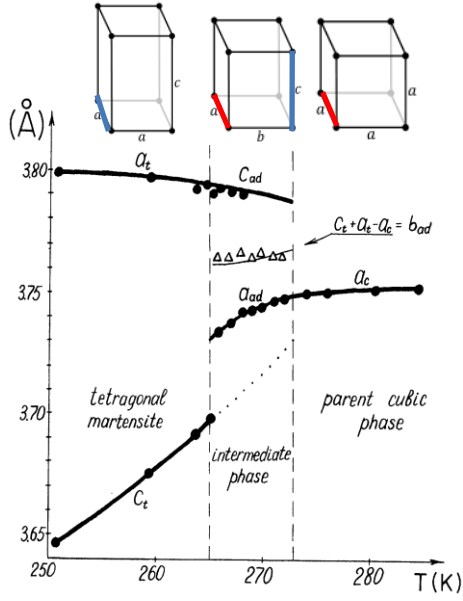
Figure 1.10: Lattice parameters in the FePd system calculated using the adaptive martensite theory of Khachaturyan (30). Data points from Seto (64). FePd has a high temperature cubic region with lattice parameter a_C and a low temperature martensite with lattice parameters a_t and c_t. An adaptive intermediate phase of orthorhombic symmetry with lattice parameter a_{ad} shared with a_c, lattice parameter c_{ad} shared with a_t, and lattice parameter b_{ad}.

For ferroelectrics the concept of adaptive martensite is useful to describe the region around the MPB. The lattice parameters in the ferroelectric adaptive state are determined by the volume fraction, ω, of each orientational variant. The volume fraction is now a function of the external electric field indicating the lattice parameters are a function of the applied field. If we consider two orthogonally oriented variants as in the above case we can arrive at the stress free strain tensor

$$\langle \varepsilon(\omega) \rangle = \omega \varepsilon(1) + (1 - \omega)\varepsilon(3)$$

$$= \frac{\omega}{a_c}\begin{pmatrix} c_t - a_c & 0 & 0 \\ 0 & a_t - a_c & 0 \\ 0 & 0 & a_t - a_c \end{pmatrix} + \frac{1-\omega}{a_c}\begin{pmatrix} a_t - a_c & 0 & 0 \\ 0 & a_t - a_c & 0 \\ 0 & 0 & c_t - a_c \end{pmatrix}. \quad (1.7)$$

Solving for the adaptive lattice parameters we obtain

$$a_{ad} = a_t + (c_t - a_t)\omega(x, E)$$

20

$$b_{ad} = a_t$$

$$c_{ad} = c_t - (c_t - a_t)\omega(x, E). \tag{1.8}$$

The parameters a_{ad} and c_{ad} are now functions of $\omega(E)$. By adding a_{ad} and c_{ad} the general

invariance condition for any value of ω is found

$$a_{ad} + c_{ad} = a_t + c_t. \tag{1.9}$$

This condition is important because it is not influenced by any external electric field.

However, full elimination of the transformation induced stress is only accomplished

when one lattice parameter from the parent phase is related to the tetragonal phase via the

invariant plane strain. In order to accomplish this misfit stresses along the habit plane

must be eliminated by choosing a special value of ω which is defined as

$$\omega = \omega_0 = \frac{a_t - a_c}{a_t - c_t}. \tag{1.10}$$

This is known as the special invariance condition and leads to the lattice parameters

$$a_{ad} = a_c$$

$$b_{ad} = a_t + c_t - a_c$$

$$c_{ad} = a_t \tag{1.11}$$

which are equivalent to the lattice parameters from the ferroelastic case since the special

invariance condition requires the absence of an electric field. If an electric field is present

the special invariance condition does not apply, however, the general invariance

condition remains applicable.

The resulting composition dependent lattice parameters between tetragonal and

rhombohedral phases are shown below in Figure 1.11. The experimental data reveals the

intrinsic relationships between lattice parameters still hold in this case as indicated by the

calculated lines. The intermediate monoclinic like phase acts as a structural bridge between the tetragonal and rhombohedral phases.
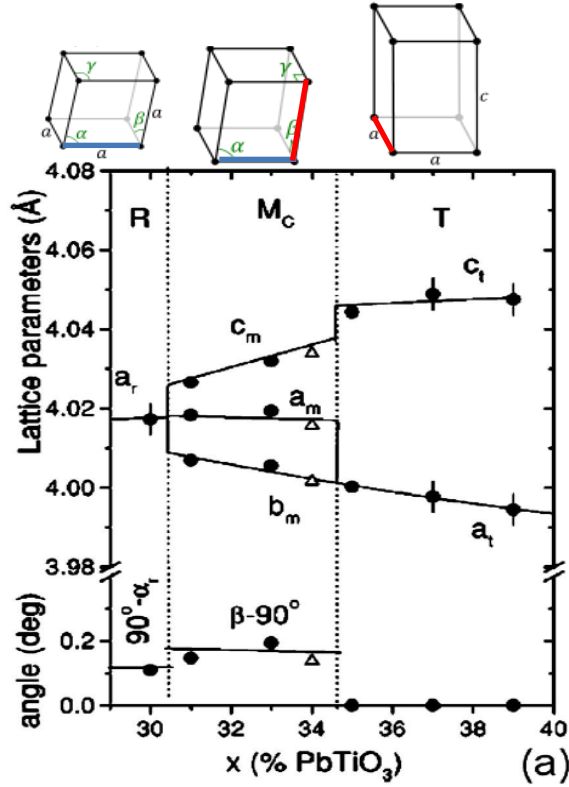
Figure 1.11 Lattice constants of PMN-xPT at 300K calculated using adaptive theory. Data points are taken from Noheda **(65)**. The intermediate monoclinic like phase acts as a structural bridge between the two low temperature phases as it shares a lattice parameter with each phase.

Recent work by Schonau et al. (31) using high resolution TEM produced the first direct experimental evidence of the existence of nanotwins in PZT near the MPB. These nanotwins change size along the MPB as the structure adapts to accommodate the phase change from rhombohedral to tetragonal.

1.4   Magnetostriction and MPB in Terfenol-D

Magnetostriction is the change in shape of a ferromagnet under an applied magnetic field. Magnetostriction is analogous to the electrostriction effect mentioned earlier in ferroelectrics (11). The magnetic field causes the domains walls to move and the magnetization to rotate producing a change in shape of the material. As the magnetic field is increased the magnetostriction increases to its maximum value λ, the saturation magnetostriction. The total strain measured in a completely saturated crystal is

$$\left(\frac{\Delta l}{l}\right)_{sat} = e. \tag{1.12}$$

Given a perfect sphere the strain along a line an angle φ from the direction of the saturation magnetostriction equals

$$\frac{\Delta l}{l} = e \; cos^2\varphi. \tag{1.13}$$

If the sphere is demagnetized magnetization is distributed at random and the strain is the average deformation given by

$$\left(\frac{\Delta l}{l}\right)_{demag} = \int_0^{\pi\backslash 2} e \; cos^2\varphi sin\varphi d\varphi$$

$$= \frac{e}{3}. \tag{1.14}$$

The magnetostriction can thus be related to the total strain by

$$\lambda = \left(\frac{\Delta l}{l}\right)_{sat} - \left(\frac{\Delta l}{l}\right)_{demag} = \frac{2e}{3}. \tag{1.15}$$

This is an important note as a measurement from a strain gauge provides a value for λ while diffraction provides a value for e.

Magnetostrictive materials are desired candidates for transducers although the effect is small in most ferromagnetic materials. Magnetostriction is measured in parts per million (ppm), or micro-strain ($\mu\varepsilon$), with typical values on the order of a few tens of $\mu\varepsilon$ up

23

to several hundred $\mu\varepsilon$ (Fe=-9, Ni=-35, Co=-62, $CoFe_2O_4$=-110) (1). In the early 1960's it was reported that at cryogenic temperatures Ho and Dy displayed magnetostrictions on the order of 1% or $10^4\mu\varepsilon$ (32). These large values of magnetostriction are caused by the additional orbital motion allowed to the 4f electrons in the rare earths. Studies were performed by Clark to alloy the rare earths with traditional magnetic transition metals aimed at finding an alloy with a higher Curie temperature but retaining the large magnetostriction of the rare earths. Of these alloys $TbFe_2$ displayed the largest known room temperature magnetostriction to date of $\sim$2500 $\mu\varepsilon$ (33). In order for this magnetostriction to be useful for a transducer and in other applications, its very large magnetocrystalline anisotropy (K_1) needed to be minimized. Therefore an alloy was created with $DyFe_2$ because $DyFe_2$ possesses a relatively low magnetostriction but has a positive K_1 while $TbFe_2$ is characterized by a negative value of K_1. Clark's work resulted in large values of magnetostriction in TDF73 at comparatively small applied fields stemming from the low anisotropy ($K_1 \approx 0$) (1), displayed in Figure 1.12.
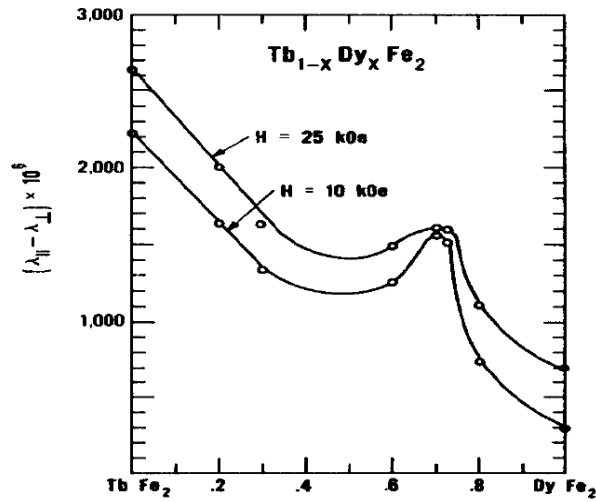
Figure 1.12: Composition dependence of magnetostriction in Terfenol-D alloys. Low anisotropy around $Tb_{27}Dy_{73}Fe_2$ yields a peak in the magnetostriction (**1**).

Alloys of TDF70, sometimes specifically named Terfenol-D, are now used in actuators and other devices due to the large magnetostriction and relatively low anisotropy ($K_1 \approx 0$) (2). In order to explain the low anisotropy a theory needed to be developed. The first theory, based on slowly rotating spins from the [100] to [111] direction, was proposed by Atzmony et al. who used crystal field theory to calculate the directions of easy magnetization at a given composition and temperature. By assuming

the direction of easy magnetization varies from the [111] to [110] along [uuv] directions then from the [110] to [100] along [uv0] directions they were able to calculate the lowest energy state along ~30 predefined directions to find the temperature dependence of the easy direction (26). A similar calculation including only [uuv] directions is displayed in Figure 1.13. These calculations reproduce the basic features in the spin transition region
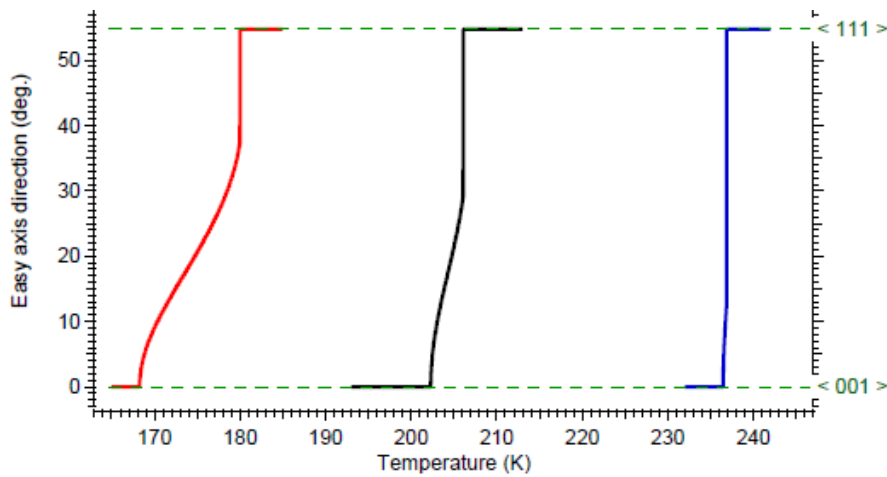
Figure 1.13 Calculated temperature dependence of the easy direction for TDF60, TDF65, and TDF70. Courtesy of Mark Laver.

as measured by Mössbauer spectroscopy Figure 1.14 (left curve). Williams et al. (34) refined the theory by adding the magnetoelastic terms to the Hamiltonian used in the crystal field calculations. Magnetostriction anisotropy is normally orders of magnitude less than magnetocrystalline anisotropy, so it is normally neglected. In this case since the magnetocrystalline anisotropy is very low near the phase transition the anisotropy energy from magnetostriction becomes significant. These results, Figure 1.14 (center), match closely with the data obtained from Mössbauer spectroscopy, Figure 1.14 (right-data points).
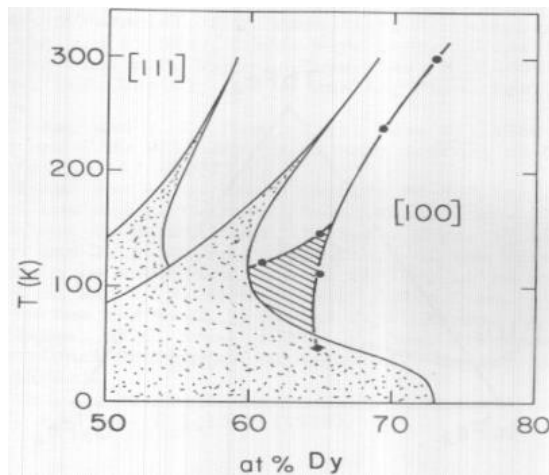
Figure 1.14 Calculated magnetic spin transition region using only crystal field effects (left) and crystal field plus magnetostriction (center) **(34)**. These calculations are compared to the easy direction calculated from Mössbauer measurements (right).

These calculations assume the transition is a second order rotation of the magnetic moment. The fundamental difference between the work reported by Ren (9) and the reports by Atzmony (5; 26) is that the transition is first order if two distinct phases coexist at certain temperatures. In the ferroelectric case the structural rigidity provides a purely elastic boundary between the two phases. In ferromagnets, however, domains of [111] easy axis and domains of [100] easy axis can relax because of the finite anisotropy, producing a MPB that changes with the temperature of the transition. *The objective of this thesis is to explore how this accommodation of the two phases changes with the temperature of the phase transition by probing several Tb$_{1-x}$Dy$_x$Fe$_2$ alloys with high resolution synchrotron diffraction at various temperatures.*

1.5   Organization of this thesis

Chapter 2 will begin with a brief outline of the magnetic properties of the samples. Magnetization and magnetostriction were measured as a function of applied field at different temperatures, M(H) and μ(H) at a given T, and magnetization was measured at constant field and varying temperature, M(T). Magnetization measurements were performed using a Lakeshore 7407 VSM and a Quantum Design SQUID while magnetostriction measurements were performed using strain gauges inside of a 1 Tesla electromagnet.

Chapters 3 and 4 deal with high resolution synchrotron and neutron powder diffraction data taken at the Advanced Photon Source (APS) and the Spallation Neutron Source (SNS) respectively. Synchrotron powder diffraction patterns provide detailed information about the structure of the alloys at the highest possible resolution. Neutron powder diffraction patterns provide information about the structure and the magnetic moments but with slightly lower resolution. Rapid scans at beamline 11-BM at APS were carried out while the temperature was constantly ramped to locate phase changes. After this high resolution powder diffraction patterns were taken in each region at several different temperatures for each sample on 11-BM and POWGEN at SNS. While the data taken at 11BM could distinguish between cubic and rhombohedral phases the data from POWGEN could not. Therefore, all samples were refined as cubic. Each of the synchrotron powder diffraction patterns were fitted to tetragonal, rhombohedral, cubic, as well as several combinations of two phase structures and several combinations of three phases in the transition region (2 Cubic + 1 Rhombohedral and 2 Rhombohedral + 1 Cubic). POWGEN data was analyzed to see how the structure change affected the

magnetic properties. Magnetic moments were refined and plotted as a function of temperature. Unfortunately, the resolution was not sufficient to obtain information about the magnetic direction.

Chapter 5 provides a summary of all of the data presented in the previous chapters. A general overview of the results is put into context with the current literature. Conclusions are drawn and future research options are presented.

Chapter 2: Macroscopic Magnetic Characterization

2.1   Overview

In this chapter, macroscopic magnetic characterization of the TDF alloys will be performed to investigate how macroscopic properties are affected by the presence of the MPB. Magnetization versus field, M(H), will be measured to ensure sample properties agree with expected values from the literature. Magnetization versus temperature, M(T), will be measured at high applied magnetic field to identify the T_C and to ascertain it agrees with reported values for these alloys. M(T) at low field will be measured to identify how the macroscopic susceptibility, χ, changes as the tetragonal to rhombohedral phase transition temperature increases. Magnetostriction will be measured to create a rough phase diagram of the TDF system and to further verify if values obtained agree with those from previous reports (1).

Eight alloys of TDF were prepared at the Metals Preparation Center at Ames Laboratory. Alloys were prepared by arc melting the constituent elements on a water cooled copper hearth plate in a high purity argon atmosphere. The starting metals were Ames Lab 99.99% pure Tb and Dy and 99.95% pure electrolytic Fe. Each alloy button was melted three times to ensure homogeneity. The specific alloys prepared were TDF65, TDF67.5, TDF70, TDF72.5, TDF75, TDF76.5, TDF78, and TDF80.

2.2   Magnetization

Samples were sealed into tantalum lined quartz capillaries and annealed at 800C for ~150 hours to further homogenize the Laves phase. Initial M(H) data was taken on

polycrystalline samples. For the rest of the data 5-10 grams of each sample was ground into a powder thoroughly by mortar and pestle and ~.02 grams of each sample was weighed out to measure the magnetization in the Vibrating Sample Magnetometer (VSM) and Superconducting QUantum Interference Device (SQUID).

2.2.1   VSM/SQUID

The VSM is an instrument where the sample is placed in the center of an electromagnet attached to a long rod which is being vibrated by a head drive in a direction perpendicular to the applied magnetic field. Faraday's law of induction states the voltage observed in a coil is proportional to the changing magnetic flux e.g.

$$V \propto \frac{dB}{dt}. \tag{2.1}$$

The magnetization can then be measured in this setup with specially designed coils on the sides of the electromagnet with the relation

$$\Delta B = \mu_0 M, \tag{2.2}$$

where μ_0 is the permeability of free space and M is the sample magnetization. Therefore, a coil with n turns of cross sectional area a has a voltage given by the relation

$$V = -na\mu_0 M/dt \tag{2.3}$$

The instrument used to collect data for these experiments is a Lakeshore model 7407 VSM (35). This VSM can be fitted with a heater or a cryostat to produce sample environments in the temperature range of 4-1300K with a noise floor of $1*10^{-7}$ emu at 10s per data point. Such a wide temperature range combined with a quick and effective way to measure magnetization under applied fields makes this the ideal instrument for rapid throughput of magnetization studies.

31

The SQUID is an extremely sensitive magnetometer that employs Josephson junctions to measure sample magnetization. The basic design of a SQUID involves running a current through a superconducting wire that splits into two current carrying superconducting wires each with their own Josephson junction. It is extremely sensitive to induction since the currents on either side change as a function of induced current. Minute changes in magnetization can be measured by a superconducting wire on the side of the sample chamber which has three coil sections and acts as a second-order gradiometer (36). The particular SQUID used for data collection in this thesis is a Quantum Design MPMS with the EverCool attachment (37).

2.2.2   M(H) and M(T) Data and Analysis

M(H) and high temperature M(T) data were taken using the VSM. Cryogenic M(T) curves were taken with the SQUID. M(H) curves are taken in continuous acquisition mode which indicates the field is continuously ramped while the moment is measured and then averaged over a period of 10s/point. M(H) data are usually taken from -10^4Oe<H<10^4Oe. At higher fields data points are averaged over 200Oe while at lower fields between -10^3Oe<H<10^3Oe data points are averaged over 50Oe or closer depending on the measurement. M(T) data are taken from room temperature to a maximum of 450C with an applied field that saturates the sample (10^4Oe) and at lower fields as indicated (500Oe, 100Oe, etc.). Data is acquired point by point meaning that the temperature is ramped to a certain value and allowed to settle before the moment is measured. The high temperature M(T) data points were taken every 10C. M(T) curves taken in the SQUID

were obtained at high $(2x10^4 Oe)$ and low fields (100Oe) from 10K to 300K with steps of 2K around the MPB region and 10K outside of the MPB region.

Magnetization was measured for each TDF alloy in the VSM. M(H) data were taken on polycrystalline samples at room temperature Figure 2.1. The datasets show magnetization values of ~70 emu/g for all compositions which agrees with published values for an alloy of $TbFe_2$ and $DyFe_2$ (1). The shapes of the curves are affected by the change in anisotropy near the transition region and shape anisotropy. The M(T) data at high temperature was also taken on the VSM. It was found that even under vacuum the rare earths rapidly oxidize at temperatures above 100C. Therefore, to prevent sample
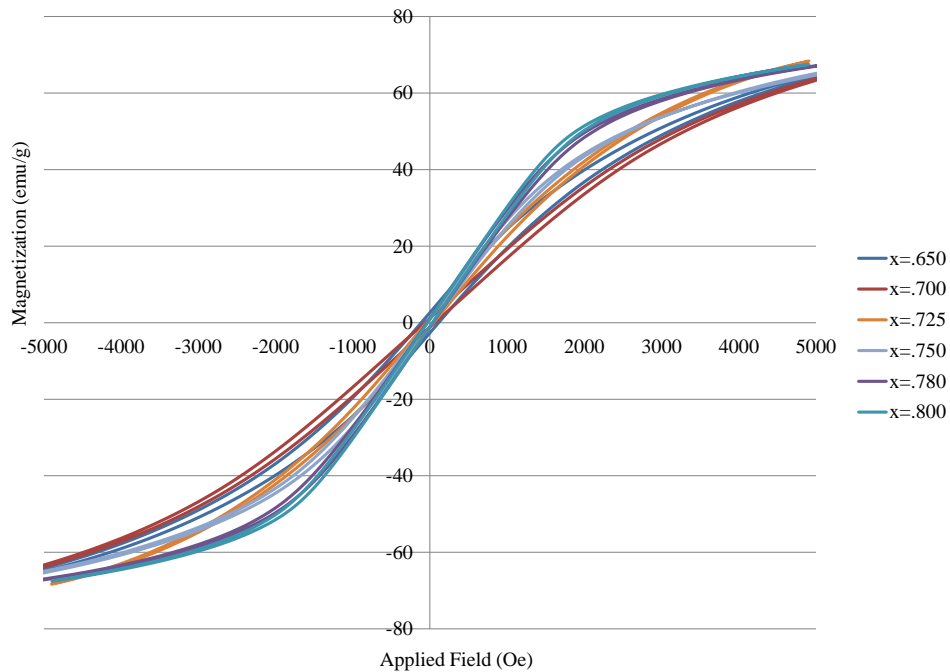
Figure 2.1: M(H) data for various TDF alloys at room temperature.

oxidation it was necessary to encapsulate the samples into quartz tubes. Powders were ground with mortar and pestle and sealed into tiny (1mm ID x 2mm OD) evacuated quartz capillaries. The high temperature M(T) for TDF 65 is displayed in Figure 2.2.

$T_C \approx 670K$ can be extrapolated from an alloy of $TbFe_2$ with $T_C=710K$ and $DyFe_2$ with $T_C=650K$ (38) and agrees with a recent report on other TDF alloys (39). The small magnetization above T_C can be attributed to tiny amounts of metallic iron from RE oxidation as the vacuum was not perfect in the sealed capillary.
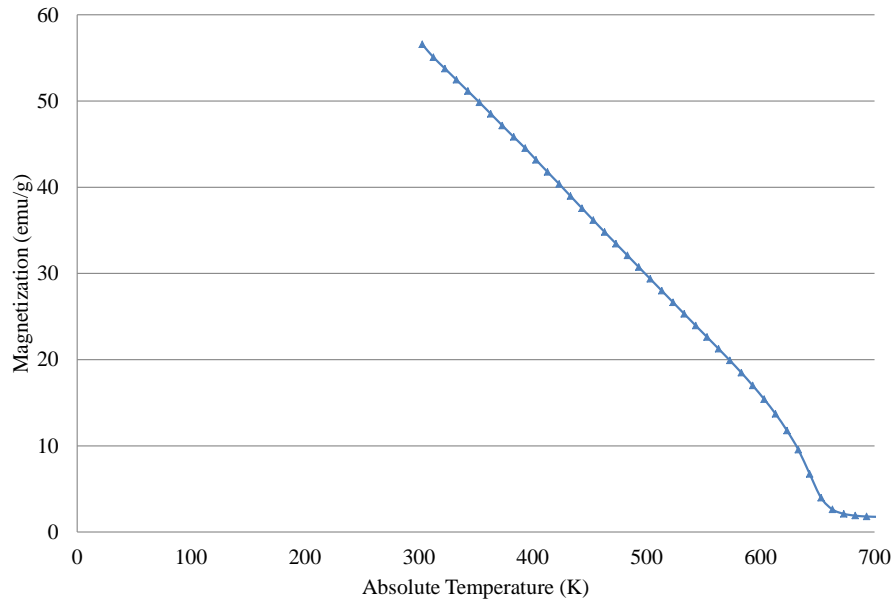
Figure 2.2: M(T) of TDF65 taken at 10k Oe. $T_C=670K$ agrees well with the literature.

The SQUID magnetometer was utilized to take M(T) data for alloys with a transition temperature below room temperature. Analyzing the data an interesting feature is apparent as the temperature of the phase transition increases. Figure 2.3 displays M(T) curves taken at $2\text{x}10^4$Oe and 100Oe for TDF65. The M(T) at high field behaves exactly as one would expect from a ferrimagnetic material with a slow decay in the magnetization as the temperature increases. This reinforces the fact discussed later in
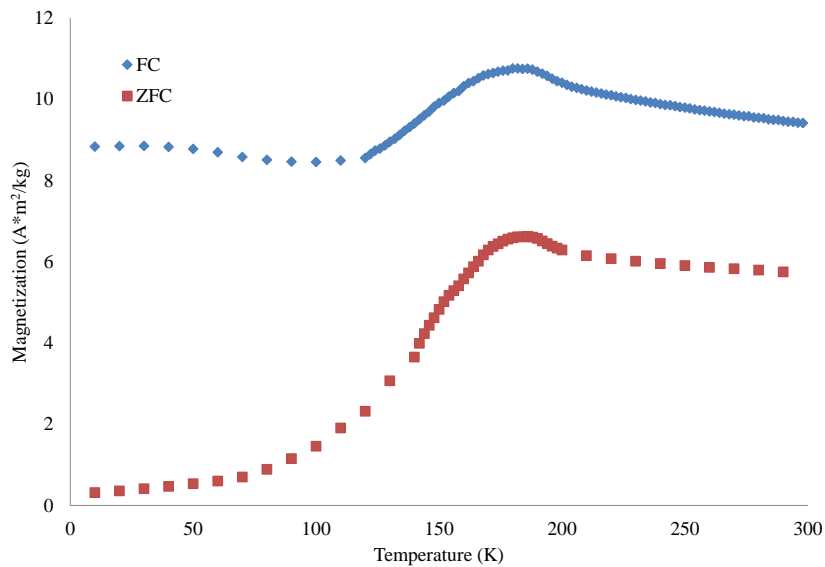
Figure 2.3: M(T) of TDF65 with 20k Oe (red squares) and 100 Oe (blue diamonds) applied fields.

(Chapter 4) that the overall magnetization is not affected by the change in symmetry at the MPB. Low field M(T) datasets produce the most interesting result, Figure 2.4. In the TDF65 sample the magnetization exhibits a sharp maximum indicating the MPB region is narrow in temperature. In the TDF70, and TDF72.5 samples a much broader maximum exists indicating the MPB region is wider in these alloys. Broadening of the maxima can be interpreted as a wider region of two phase coexistence at higher temperatures.
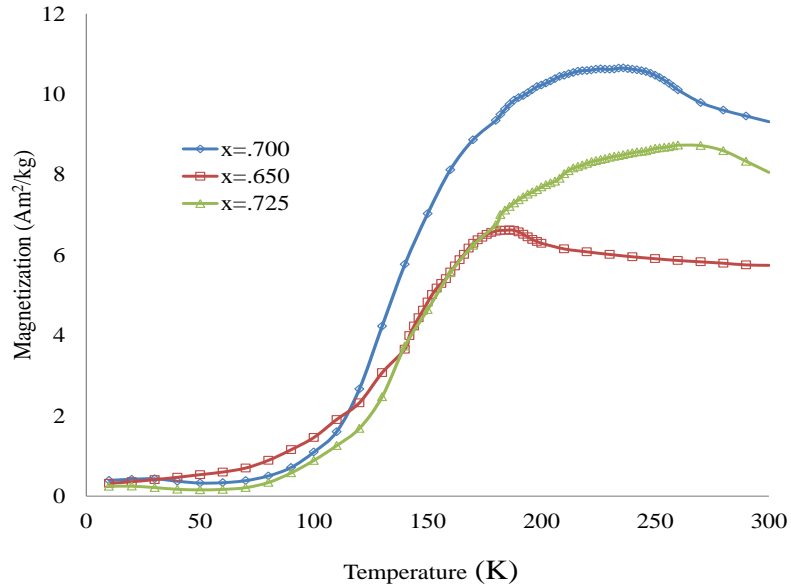
Figure 2.4: M(T) plots of TDF65 (red squares), TDF70 (blue diamonds), TDF72.5 (green triangles) taken at 100 Oe applied field.

2.3   Magnetostriction

As-received arc melted samples were cut and rough polished into circular pieces ~1.5 cm diameter and .5 cm thick. Samples were then finely polished to ensure a good mating surface between the sample and the strain gauge and to further reduce sample thickness. Micro Measurements model WK-13-031CF-350 high temperature strain gauges were then attached orthogonally to either side of the sample using M-bond 600 adhesive. Samples were then placed inside a 1 Tesla electromagnet where magnetostriction was measured as a function of field ($\mu(H)$) parallel and perpendicular to the magnetization direction at various temperatures from room temperature up to 200C Figure 2.5. The curves below are plotted by taking the difference between $\mu\varepsilon_{parallel}$ and $\mu\varepsilon_{perpendicular}$. Results of the measurements at room temperature closely match the work by Clark (1). Peak values of magnetostriction decrease as $DyFe_2$ concentration is increased

as expected by the much higher magnetostriction of $TbFe_2$ than $DyFe_2$ simply considering alloying.
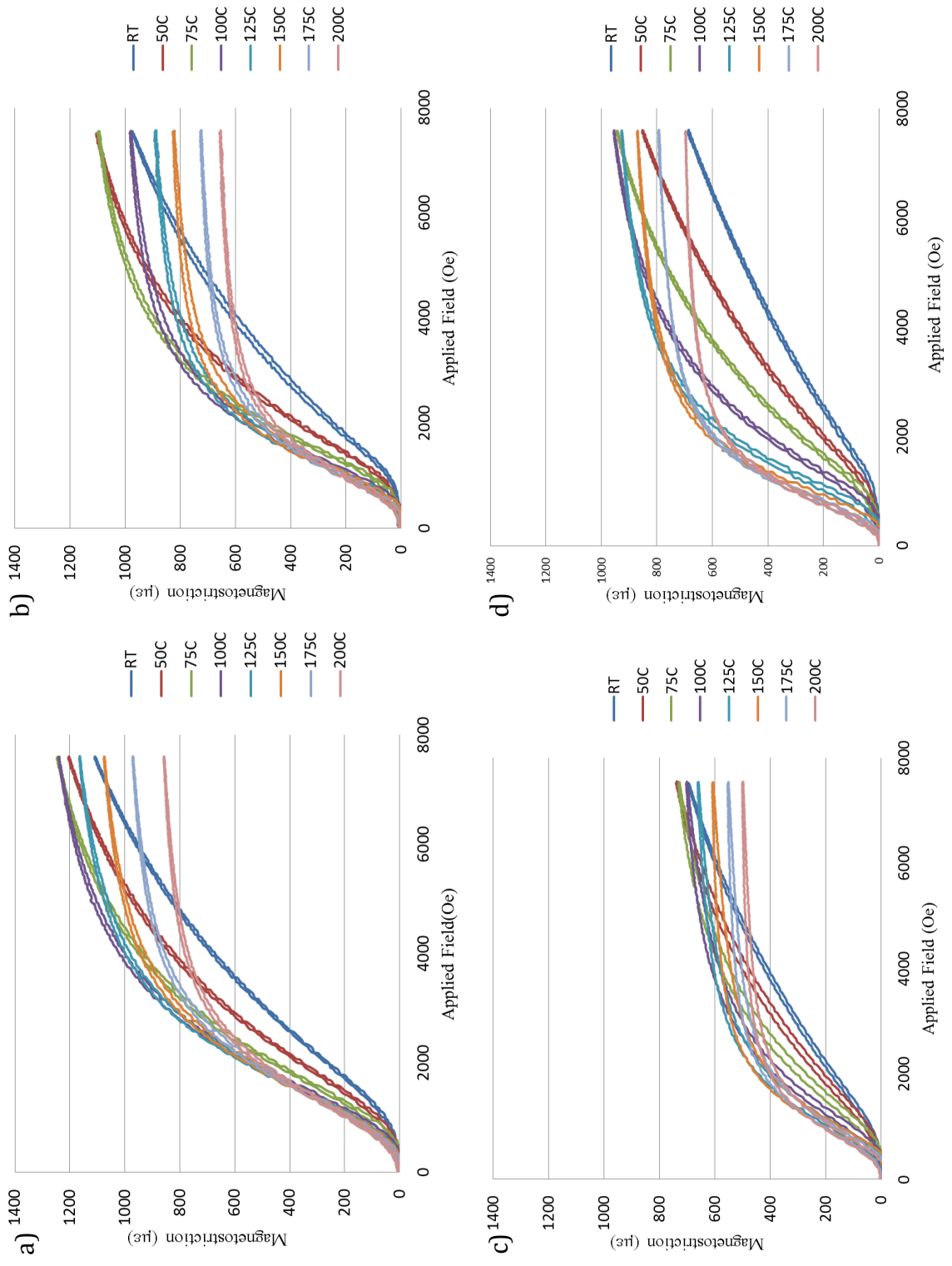
Figure 2.5: Magnetostriction plots ($\mu\varepsilon_{parallel}$ - $\mu\varepsilon_{perpendicular}$) of (a) TDF75, (b) TDF76.5, (c) TDF78, and (d) TDF80 as a function of temperature. Note: Poor strain gauge mating likely affected data on TDF78.

When graphing the maximum slope of the magnetostriction, the amount of length change per unit of magnetic field applied, we see definite peaks at progressively higher temperatures as the fraction of Dy is increased, Figure 2.6. We suspect that the peaks of the magnetostrictive susceptibility are located at a temperature where the MPB is present due to a minimum in the anisotropy when the six easy [100] directions and the 8 [111]
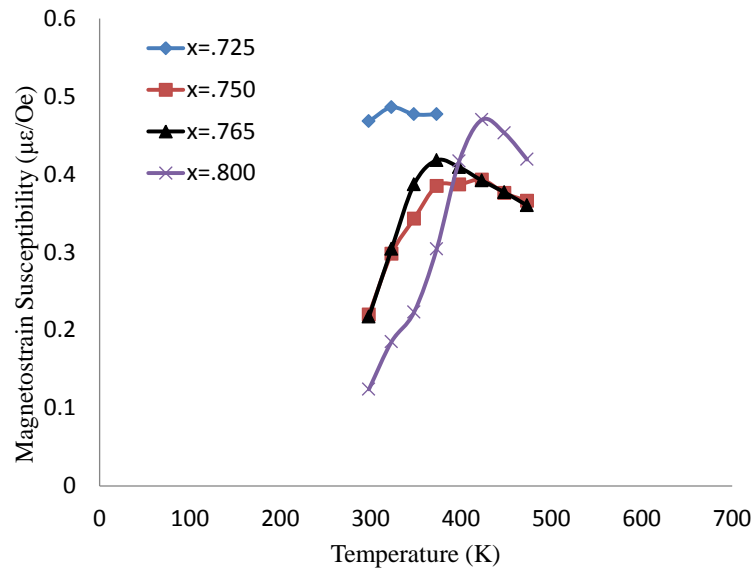
Figure 2.6: Magnetostriction susceptibility of various Terfenol-D alloys as a function of temperature. The maxima are suspected to be at the temperatures where MPBs are present. As $DyFe_2$ volume fraction increases the maxima shift to higher temperatures.

directions coexist. At lower temperatures we expect to find a tetragonal phase and at higher temperatures a rhombohedral phase. Using this reasoning a proposed phase diagram with a linear extrapolation from 0K to the Curie temperature has been plotted Figure 2.7. This data has been compared to the findings of Atzmony et al. who used Mössbauer spectroscopy to find the magnetic easy directions (26) and agrees satisfactorily with the transition region shown in Figure 1.7. The softening of the

magnetocrystalline anisotropy at the phase transition is direct evidence that this transition is magnetoelastic.
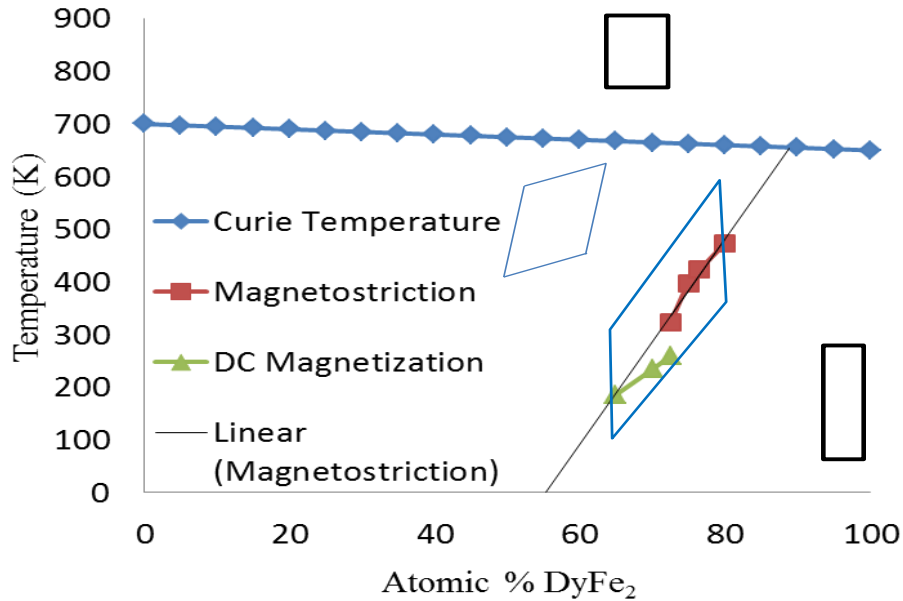
Figure 2.7: Proposed phase diagram of TDF with a high temperature cubic phase and two low temperature phases rhombohedral on the $TbFe_2$ side and tetragonal on the $DyFe_2$ side. Data points extracted from the maxima of the magnetostrictive susceptibilities and the maxima of the DC magnetization studies performed in the SQUID and the line is a linear extrapolation of the maxima of the magnetostrictive susceptibilities. The blue square highlighting the area of interest for synchrotron and neutron powder diffraction studies is shown.

2.4   Conclusions

The macroscopic magnetic properties of the TDF alloys were characterized using VSM, SQUID, and strain gauges under various conditions. The properties that have previously been reported in the literature are reproduced in the TDF alloys we measured. Overall, the findings indicate a transition region that is rapidly increasing in temperature as composition of $DyFe_2$ is increased. The magnetization at low field in the SQUID shows a broadening of the phase transition as its temperature is increased. The proposed

explanation of this effect is a widening of the region of meta-stability of [100] and [111]

easy directions at higher temperatures.

Chapter 3: X-ray/Synchrotron Powder Diffraction

3.1   Overview

Room temperature x-ray powder diffraction (XRD) and subsequent Rietveld refinement was performed on all samples. Additional synchrotron XRD experiments were carried out at the Advanced Photon Source (APS) at Argonne National Laboratory to investigate the temperature dependence of the MPB and to gather high quality powder diffraction data for Rietveld refinement. The Rietveld data will provide details of the structure of TDF alloys when the MPB is present.

3.2   Background

The X-ray is a form of electromagnetic radiation that has a wide range of wavelengths. For crystallography the useful wavelengths are on the order of interatomic distances (.5-2.5Å). X-rays are primary method used in crystallography. The initial discovery of the X-ray was in 1895 by Wilhelm Conrad Röntgen for which he received the first Nobel Prize in 1901 (40). X-rays cannot be focused or de-focused so for most uses they cannot directly image a structure. This is unlike other techniques, such as TEM, which allows a direct visualization of a structure since the electron can be focused and de-focused with magnetic lenses. What X-rays can do is diffract off of a crystal lattice and produce an intensity pattern in reciprocal space. This pattern can then be transformed into a crystal lattice only after a Fourier transformation is applied. It is important to note that X-rays interact with electrons and are thus scattered by the electron cloud. There are other methods of diffraction which use a different probing mechanism such as the

neutron which interacts with the nucleus and the magnetic lattice which will be discussed in further detail in Chapter 4.

The topics related to X-ray powder diffraction will be introduced. For a more thorough description of diffraction and general X-ray physics the reader is referred to the following texts (41; 42; 43). For X-ray powder diffraction, which this introduction is based, see the following text (44). When X-rays are incident on a material several processes are observed, coherent scattering, incoherent scattering, and adsorption. For practical purposes we will only consider coherent scattering. There are two ways to model X-ray diffraction the kinematic and the dynamic approaches. Kinematic theory only allows for one scattering event per X-ray while dynamic theory allows for multiple scattering events per X-ray. Dynamic scattering significantly increases the mathematical complexity of diffraction theory. Powders and most imperfect crystals meet several conditions that limit dynamic interactions including small sized crystallites and sufficient misorientation between the crystallites. For this reason only the kinematical model will be discussed here.

X-rays interact with electrons and are thus scattered by the electron cloud. When an X-ray interacts with an electron it scatters a spherical wave, known as coherent scattering. The spherical wave derives from the fact that X-rays are a form of electromagnetic (EM) radiation that possess an oscillating EM field. The electron is subjected to this EM field and through its acceleration and deceleration emits coherent radiation. Considering multiple electrons arranged in a periodic linear array each would scatter a spherical wave that interferes constructively and destructively at certain points in space with a total intensity

$$I(\varphi) \propto \frac{sin^2 N\,\varphi}{sin^2 \varphi}, \tag{3.1}$$

where N is the number of electrons and φ is the phase angle defined as

$$\varphi = 4\pi a \frac{sin^2 \theta}{\lambda}, \tag{3.2}$$

where a is the distance between neighboring electrons and θ is the scattering angle. As the number of electrons, N, approaches infinity the intensity becomes a delta function with intervals of π. In a crystal with a large number of electrons diffraction patterns have spacings related to the distance between scattering centers.

Atoms have a radial distribution of electrons which creates a path difference between scattered X-rays at values of $\theta > 0$. Therefore, atoms cannot be described as point scattering centers instead the intensity scattered from an atom is the previously derived expression for scattering from an electron modified by a decaying function, known as the atomic scattering function, f. The mathematical description of the intensity including the atomic scattering function is as follows

$$I(\varphi) \propto f^2(\varphi) \frac{sin^2 N\,\varphi}{sin^2 \varphi}. \tag{3.3}$$

The final step is to consider scattering from a lattice. The lattice is a three dimensional structure so we must consider three dimensions with discrete values for intensity maxima as follows

$$I(\varphi) \propto f^2(\varphi) \frac{sin^2 N_1\,h\pi}{sin^2 h\pi} \frac{sin^2 N_2\,k\pi}{sin^2 k\pi} \frac{sin^2 N_3 l\pi}{sin^2 l\pi}. \tag{3.4}$$

In most cases the unit cell is made of multiple different types of atoms so the atomic scattering factor should be replaced with a structure factor, F, which describes the scattering from all atoms in the unit cell

$$I(hkl) \propto F^2(hkl) \frac{sin^2 U_1\,h\pi}{sin^2 h\pi} \frac{sin^2 U_2\,k\pi}{sin^2 k\pi} \frac{sin^2 U_3 l\pi}{sin^2 l\pi}, \tag{3.5}$$

44

where N has been replaced by U_x, the number of unit cells in each direction, and φ has been replaced by hkl.

Diffraction off of crystals by X-rays was first observed by Laue in 1912. Laue observed that certain conditions were met at the peaks of the diffraction pattern, described by the equations

$$a\big(cos(\Psi) - cos(\varphi_1)\big) = h\lambda$$

$$b\big(cos(\Psi) - cos(\varphi_2)\big) = k\lambda$$

$$c\big(cos(\Psi) - cos(\varphi_3)\big) = l\lambda. \tag{3.6}$$

A year later Sir William Lawrence Bragg introduced the Bragg conditions of diffraction, which follow from the Laue conditions. Bragg described the diffraction from a periodic crystal with the formula

$$n\lambda = 2d_{hkl}sin\theta_{hkl}, \tag{3.7}$$

where n is an integer, λ is the wavelength of the X-ray, d is the spacing between planes, and θ is the angle of incidence.

Since diffraction from crystals produces a pattern in reciprocal space a visual representation of reciprocal space is a useful tool for analyzing diffraction patterns. This visual representation of reciprocal space was introduced by P.P. Ewald. Ewald proposed that if we set the length of the propagation vector, k_0, to the inverse of the wavelength

$$|k_0| = \frac{1}{\lambda}, \tag{3.8}$$

a wave with this wavevector incident on a crystal will produce a scattered wave, k_1, with the same wavelength and an angle between k_0 and k_1 of 2θ. If we set the end of the propagation vector, k_0, to the origin and then rotate the vector k_1 freely in all directions a sphere in reciprocal space is formed. This sphere is known as Ewald's Sphere and

45

diffraction can only be observed when a reciprocal lattice point intersects the surface of the sphere.

Two X-ray diffraction techniques are widely utilized, single crystal and powder diffraction, each with its own advantages and limitations. While single crystal diffraction is usually preferred it can be impractical for certain materials. This is especially true for materials which possess challenging or technologically impossible growth methods for large single crystals. Under these circumstances the only choice is to perform X-ray powder diffraction.

Powder diffraction is a technique performed on finely ground powders with crystallite sizes in the μm to sub μm range. Monochromatic X-rays incident on the sample are exposed to many crystallite orientations simultaneously. Since the orientation of each crystallite is random the reciprocal lattice orientation is also random which implies that diffraction off a sufficiently large number of crystallites accounts for every possible orientation. The diffraction off a powder sample can be visualized by a cone with a ring on the Ewald sphere which has an angle of 4θ. Assuming that the orientation is truly random the rings will have equal intensity around the entire circumference. This fact allows a detector to be made that only takes the spectrum at a small section of the ring and along an equidistant arc in the 2θ direction. For practical purposes there is only one independent variable in X-ray powder diffraction, the angle 2θ. A typical powder diffraction pattern is plotted as the relative intensity vs. 2θ or if one is looking for consistent data among X-ray sources with different incident wavelengths relative intensity can be plotted against Q which is represented mathematically by

$$Q = \frac{2\pi sin\theta}{\lambda}. \hspace{4cm} (3.9)$$

Powder diffraction patterns are composed of four components the positions, intensities, shapes of the peaks, and the background. Peak positions are determined from the Bragg condition of diffraction. This implies the position of a given reflection can be determined using the wavelength of the incident radiation, the unit cell parameters (a, b, c, α, β, γ), and the *hkl* indices of the plane. The intensities of the reflections are based on the structure factor and the number of unit cells in each crystalline direction. It is important to note that the structure factor will make certain peaks extremely small or even invisible. The shapes of the peaks are determined by the instrument parameters such as spectral dispersion and geometry as well as minor contributions from the sample such as impurities and strain. If we combine the positions, intensities, and shapes of the peaks we can construct a diffraction pattern after adding in the underlying background. Each of the contributing factors to peak position, intensity, and shape is described in detail in reference (44) Chapter 8.4-8.6 and will be discussed later.

3.2.1   Rietveld Refinement

Whole pattern refinement or Rietveld refinement was first reported by Hugo Rietveld in 1969 in the landmark paper "A Profile Refinement Method for Nuclear and Magnetic Structures" (45). Rietveld originally used the method to refine neutron diffraction data. He foresaw that this method could be utilized in X-ray diffraction but he never pursued this. The widespread use of Rietveld refinement for X-ray diffraction data was much slower than neutron diffraction. This is due to several factors that add increased mathematical complexity to the refinement of X-ray diffraction data. These factors include increased complexity of the peak shape functions in X-rays compared to

neutrons, angular dependent form factors, the α_1-α_2 doublet, adsorption, fluorescence in the background, and monochromation of the beam. Most of these complications are greatly diminished by the use of synchrotron radiation as an X-ray source.

The Rietveld method, in contrast to earlier methods that integrated intensities of each peak, uses each individual data point in the diffraction pattern as a separate observation. The observation can then be calculated as the sum of all reflections at that scattering angle. This was a great step forward for powder diffraction where peak overlapping becomes significant due to low instrument resolution or high symmetry of the scattering material. The pattern is refined using a least squares approach where the sum of the least squares difference at each data point is minimized simultaneously. The quantity to be minimized is

$$S = \sum_i w_i \big(y_i(obs) - y_i(calc) \big)^2 \qquad (3.10)$$

with w_i the weight of each observation, $y_i(obs)$ and $y_i(calc)$ are the observed and calculated intensity at each data point respectively. The weight of each data point is based on the squares of the standard deviation given by the quantity

$$w_i^{-1} = \sigma_i^2 = \sigma_{ig}^2 + \sigma_{ib}^2 \qquad (3.11)$$

where σ_{ig}^2 and σ_{ib}^2 are the squares of the standard deviation of the counting statistics and the background.

During Rietveld refinement variables that contribute to peak position, peak intensity, and peak shape must be refined. These parameters are refined which requires a good model with realistic starting values for most parameters to perform the refinement.

Peak positions are determined by the unit cell dimensions. The Bragg condition, Eq 3.7, rewritten

48

$$\sin(\theta_{hkl}) = \frac{\lambda}{2d_{hkl}} \qquad (3.12)$$

must be satisfied for diffraction to occur. For any given *hkl* the interplaner separation can be derived from the expression

$$\frac{1}{d^2} = [\frac{h^2}{a^2 sin^2\alpha} + \frac{2kl}{bc}(cos\beta cos\gamma - cos\alpha) + \frac{k^2}{b^2 sin^2\beta} + \frac{2hl}{ac}(cos\alpha cos\gamma - cos\beta) +$$

$$\frac{l^2}{c^2 sin^2\gamma} + \frac{2hk}{ab}(cos\alpha cos\beta - cos\gamma)]/$$

$$(1 - cos^2\alpha - cos^2\beta - cos^2\gamma + 2cos\alpha cos\beta cos\gamma), \qquad (3.13)$$

which has lattice parameters a, b, and c with angles α, β, and γ. This expression can be simplified for higher symmetry systems but for the complexity of the software the general form is most desirable. Additional parameters shift the observed 2θ values from the calculated Bragg angles. Several factors contribute to this shift and can be described as a single parameter Δ2θ. This parameter expressed in equation form is

$$\Delta 2\theta = \frac{p_1}{tan2\theta} + \frac{p_2}{sin2\theta} + \frac{p_3}{tan\theta} + p_4 sin2\theta + p_5 cos\theta + p_6, \qquad (3.14)$$

where p_1 and p_2 are parameters accounting for the axial divergence of the incident beam, p_3 accounts for the zero curvature of flat surface samples, p_4 models the adsorption of the sample, p_5 corrects for displacement from the axis of the goniometer, and p_6 accounts for a zero shift from improper alignment.

Shapes of powder diffraction peaks are dependent on multiple variables and certain fixed instrument parameters. They are described the Peak Shape Function (PSF). The PSF is defined as a convolution of three functions plus the background. The PSF is written in equation form below

$$PSF(\theta) = \Omega(\theta) \otimes \Lambda(\theta) \otimes \Psi(\theta) + b(\theta). \qquad (3.15)$$

The three functions are from instrumental broadening (Ω), wavelength dispersion (Λ), and the specimen function (Ψ). Peak shapes can be fitted using one of three methods which follow: First, the empirical method can be used to model the PSF without using any physical parameters. Second, the semi-empirical method fits the PSF with empirical methods for the instrumental and wavelength dispersion functions and the specimen properties are fitted using physical parameters. Lastly, in the fundamental parameters method all three functions are fitted with physical parameters.

The peak shape can be described by one of four functions Gaussian, Lorentzian, Pseudo-Voigt, and Pearson-VII. In our refinements for synchrotron X-rays we will use the Thompson modified Pseudo-Voigt function (46), GSAS profile function 3. The Pseudo-Voigt function is a mixture of instrumental Gaussian and specimen Lorentzian contributions

$$y(x) = PV(x) = \eta \frac{C_G^{1/2}}{\sqrt{\pi H}} \exp(-C_G x^2) + (1 - \eta) \frac{C_L^{1/2}}{\sqrt{\pi H}} \exp(-C_L x^2)^{-1}. \qquad (3.16)$$

H is the full width at half maximum (FWHM), x describes the position of a point relative to the maximum of the peak divided by the FWHM $x=(2\theta_i-2\theta_k)/H_k$, C_G and C_L are the normalization factors for the Gaussian and Lorentzian contributions to the peak shape, and η is the mixing parameter between Gaussian and Lorentzian contributions. The Thompson modified Pseudo-Voigt function modifies H and η as follows

$$H = \left(\sum_{i=0}^{5} a_i H_G^{5-i} H_L^i \right)^{1/5} \qquad (3.17)$$

$$\eta = \sum_{i=1}^{3} b_i \left(\frac{H_L}{H} \right)^i \qquad (3.18)$$

$$H_G = 2\sigma\sqrt{2ln2} \qquad (3.19)$$

$$\sigma = \sqrt{U tan^2\theta + V tan\theta + W + P/sin^2\theta} \qquad (3.20)$$

$$H_L = \frac{X + X_a cos\phi}{cos\theta} + (Y + Y_a cos\phi)tan\theta \qquad (3.21)$$

H_G and H_L are the Gaussian and Lorentzian FWHM terms, U, V, and W are free variables fixed to instrument parameters, P is a broadening parameter, X_a and Y_a are anisotropic broadening parameters describing crystallite size and strain respectively, ϕ is the angle between the anisotropy axis and a reciprocal lattice vector, and finally X and Y are refined parameters describing specimen broadening from crystallite size and strain respectively.

Relative peak intensities are a function of the crystal structure factor, F, discussed earlier and to a lesser extent specimen properties such as preferred orientation and shape as well as instrumental factors such as the focusing geometry etc. Absolute intensity in refinement is a function of specimen size and refined as a single parameter, K, the scale factor.

3.3   X-Ray Diffraction

X-ray powder diffraction with Rietveld refinement was performed at room temperature to determine the structure of each alloy. A typical diffraction pattern is shown below Figure 3.1.
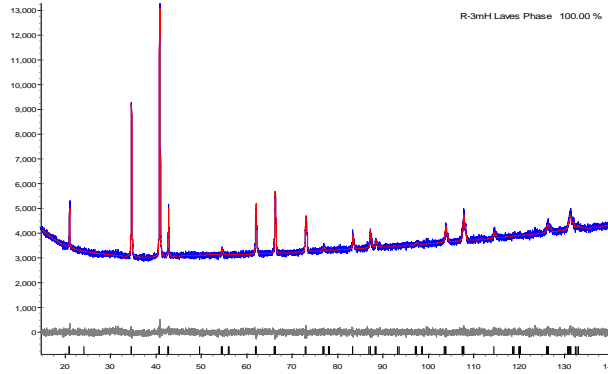
Figure 3.1: Refined X-ray diffraction pattern of Terfenol-D x=.650 sample. Refinement shows a Laves phase with rhombohedral distortion of 2482με.

TDF65, TDF 67.5, TDF70, and TDF72.5 exhibit rhombohedral distortion and the rest of the alloys TDF75, TDF76.5, TDF78, and TDF80 are cubic since the tetragonal distortion is smaller than the instrument resolution (47). Table 3.1 displays the structure and the self-strain in several TDF alloys which vary from several thousand με to essentially zero in alloys with higher $DyFe_2$ composition than TDF72.5. This suggests that a region exists between TDF72.5 and TDF75 where there is a coexistence of both phases at room temperature with MPBs separating the phases. Since these TDF alloys are within a tight range of composition we expect that the samples with lower $DyFe_2$ concentrations will have MPBs at lower temperatures and those with higher $DyFe_2$ concentrations will have MPBs at higher temperatures.

x	.65	.725	.750
Crystal Structure	Rhombohedral	Rhombohedral	Cubic(Tetragonal)
Distortion	2482με	2528με	~0με

Table 2.1: Self strain of several TDF alloys as calculated from Rietveld refinement of room temperature X-ray powder diffraction.

52

3.4   Synchrotron Powder Diffraction

Dedicated synchrotron sources were first constructed in the 1960's. They use bending magnets to accelerate electrons around a storage ring and X-rays are emitted tangentially to the orbit of the electrons. These facilities produce X-rays with both brilliance and coherence that are unmatched in laboratory X-ray instruments. Synchrotron storage rings can be quite large on the order of a km so the beam is nearly parallel which improves instrument resolution (44). Synchrotron beams are intense over a large wavelength range enabling the user the flexibility to change the wavelength between a wide range of values to suit the needs of the experiment. Synchrotron sources generally operate at a shorter wavelength than laboratory X-ray instruments which allows peaks with smaller d-spacings to be resolved and greatly reduces fluorescence (48). The high energy of the incident radiation reduces sample adsorption which can be a particular problem in materials with high Z atoms.

Several TDF alloys were used in synchrotron powder diffraction experiments at APS. Beamline 11-BM was selected for its hard X-rays ~30KeV producing a wavelength of ~.413Å. A detailed review of 11-BM is found in (49). 11-BM was designed to be a user friendly, high throughput, high resolution powder diffractometer. The beam covers an area of 1.5mm (width) by .5mm (height) at the sample. The diffraction is detected by a bank of 12 analyzer crystals with a separation of 2°. The bank can be rotated so a scan of 2° effectively covers 24°. Detectors are not identical so the software must adjust for each detector wavelength, $2(\theta)$ offset, and detector sensitivity by using NIST Si and Al_2O_3 standards for calibration (50). Also, the user must be aware of where the highest quality data is since detector coverage is not even across the $2(\theta)$ range, Figure 3.2.

Figure 3.2: Detector coverage time as a function of angle for a standard high resolution scan on 11-BM. The best statistics will be from 22-28°.

Instrument resolution can be as high as $\Delta Q/Q \approx 2.0 \times 10^{-4}$ with a minimum step size of .0001° and a detector range of .5-130°. Samples are rotated at 5400RPM in order to reduce preferred orientation. X-ray energies are tunable from 15-35KeV but data presented in this thesis was taken at 30KeV for an effective wavelength of .413Å.

Terfenol-D powders were loaded into .3mm quartz capillaries inside .8mm Kapton tubes to minimize the x-ray adsorption. A Cryostream blow type cryofurnace was utilized to vary the sample temperature between 100-450K. Two types of experiments were performed. First, quick scans (~5min) were taken while temperature was constantly ramped at 30K/hr while the detectors moved from 6-10° with a step size of .001° and a counting time of .07 sec/step. After data collection the raw data was made into a contour plot by plotting temperature on the x-axis, d-spacings on the y-axis, and color indicates intensity.
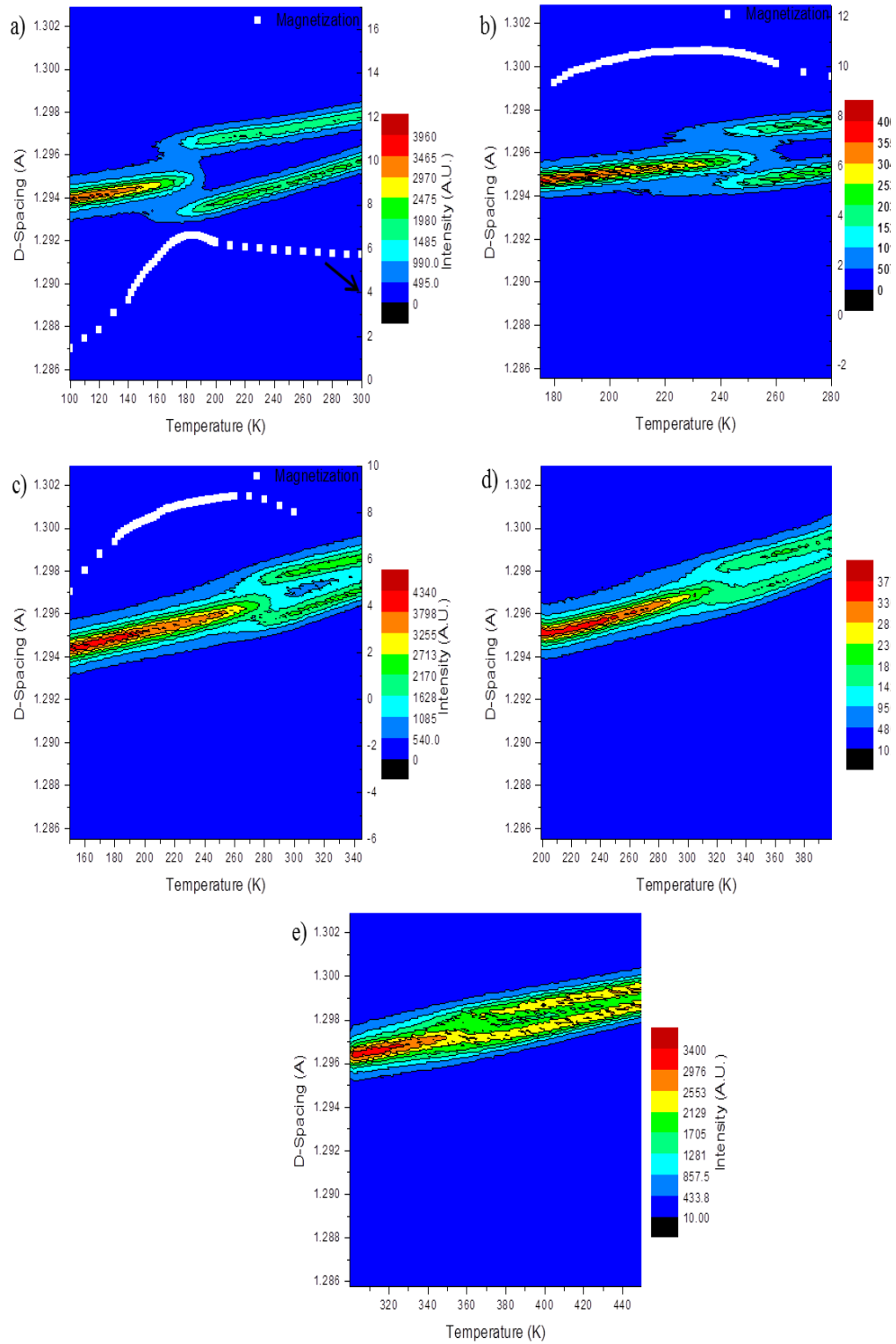
Figure 3.3: Contour plots showing d-spacing of the cubic 440 peak as a function of temperature for a) TDF65 b) TDF70 c) TDF72.5 d) TDF75 e) TDF78. M(T) plots are overlaid to show the widening of the two phase region at higher temperatures.

Contour plots of the cubic [440] peak are plotted for TDF65, TDF70, TDF72.5, TDF75, and TDF78 in Figure 3.3. With increasing temperature we can see three distinct regions: First, a single peak indicative of a cubic phase at low temperature, next it transitions into a two phase region where both cubic and rhombohedral phases are
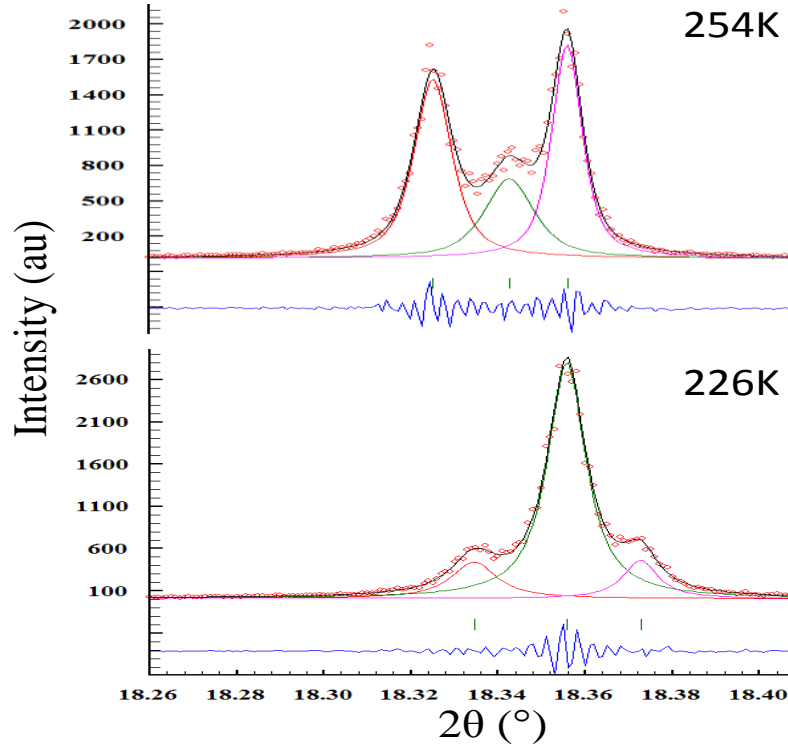
Figure 3.4: Profile fits of the 440 cubic peak for TDF70 in the two phase region. At 226K (bottom) 25% of the total intensity is from the rhombohedral peaks. At 254K (top) 75% of the total intensity in from the rhombohedral peaks.

present, and finally a pure rhombohedral phase. The center region with two phases co-existing indicates a first order phase transformation containing MPBs. To verify the coexistence of two phases systematic profile fitting was performed in WinPLOTR (51) on the 440 cubic peak to ascertain the temperature range where a non-trivial fraction (>25%) of each phase is present, displayed in Figure 3.4. Our results are very consistent with the results from of Mössbauer spectroscopy performed by Atzmony et. al. (23),

shown in Figure 3.5. In the figure we plot lines showing the region of 25-75% rhombohedral volume fraction since the peak fitting is only reliable in a region of non-trivial volume fraction of the minority phase. It is revealing to see the extent that our data can be explained by single-ion crystal field theory at low temperatures. In Figure 3.5, we plot as background shading the calculated easy axis of magnetization from the single-ion theory by minimizing the expression

$$F = (K_1 + K_{ME})\left(\alpha_x^2\alpha_y^2 + \alpha_x^2\alpha_z^2 + \alpha_y^2\alpha_z^2\right)$$

$$+K_2\left(\alpha_x^2\alpha_y^2\alpha_z^2\right) + K_3\left(\alpha_x^4\alpha_y^4 + \alpha_x^4\alpha_z^4 + \alpha_y^4\alpha_z^4\right)$$

$$+K_4\left(\alpha_x^4\alpha_y^4\alpha_z^2 + \alpha_x^4\alpha_y^2\alpha_z^4 + \alpha_x^2\alpha_y^4\alpha_z^4\right) \tag{3.22}$$
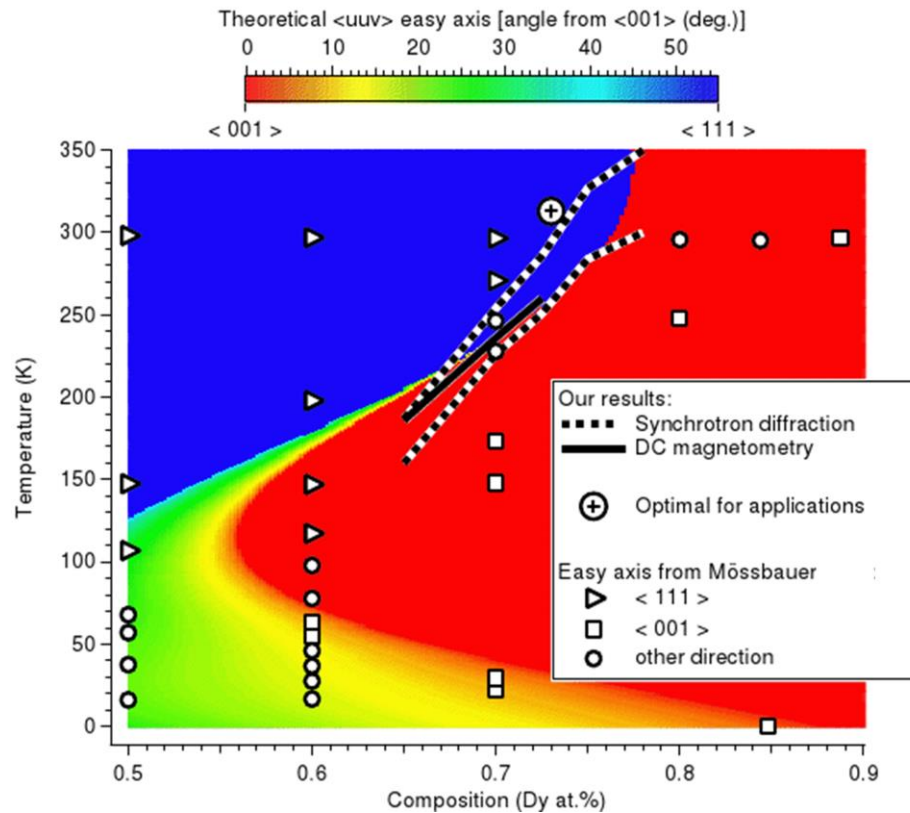
Figure 3.5: Phase diagram of the TDF system. The boundaries of the two phase region (25-75% rhombohedral phase) determined by synchrotron diffraction experiments are plotted (alternating white and black dashed lines) alongside previous Mossbauer spectroscopy measurements (triangles, squares, and circles) and are in sufficient agreement. Included is the location of the peak values of the low field magnetometry measurements (solid black line). The background shading is the calculated easy axis of magnetization from crystal field theory. Background shading courtesy of Mark Laver.

where the easy axis is described by the directional cosines α. This theory is based on the work of Callen (52; 53) and modified to include magnetostriction by Williams (34). The values of anisotropy terms included in the calculation were taken from the work of Martin (54).

We can see from Figure 3.5 that at low temperatures there is reasonable agreement between our data and the crystal field theory but at higher temperatures the MPB region begins to widen in our data while the crystal field theory predicts it will

narrow. This fact establishes a different mechanism between the high and low temperature spin transition regions in TDF alloys.

The mechanism behind the change in character of the phase transition can be understood by considering the temperature dependence of the magnetocrystalline anisotropy. The temperature dependence of the atomic shape anisotropy was given in Eq 1.4 as a function of the reduced magnetization. If we consider a cubic crystal where n=4 the atomic shape component of the magnetocrystalline anisotropy is given by

$$\frac{K_1}{K_{10}} = \left(\frac{M(T)}{M(0)}\right)^{10}.$$

(3.23)

There is a second term in the magnetocrystalline anisotropy from magnetostriction which is described by

$$\frac{K_{1magel}}{K_{0magel}} \propto \left(\frac{M(T)}{M(0)}\right)^{6}.$$

(3.24)

We can see that K_{1magel} becomes dominant as temperature increases. The sign of K_{1magel} is the same for both $TbFe_2$ and $DyFe_2$ and prefers the [111] direction. This term is responsible for the tilt of the transition region towards the $DyFe_2$ side of the phase diagram at high temperature. It materializes as K_{1magel} becomes more comparable with K_1 so more $DyFe_2$ must be added to compensate for the decreased preference it has to the [100] direction

The dramatic temperature dependence of the anisotropy means higher order anisotropy terms, such as K_3, that allow rotation of the magnetic moment from the principle axes are greatly diminished at high temperature. This leaves only K_1 and K_2 with any significant value at these temperatures. Therefore, at higher temperatures, the observed first order transition occurs because metastable domains of [111] oriented spins form, depicted in Figure 3.6. As the transition temperature increases the MPB widens in
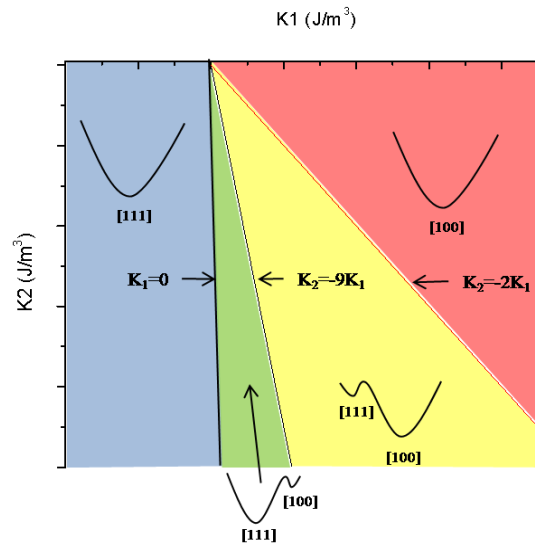
Figure 3.6: a) Diagram of the stability of the easy axis of magnetization based on (27). Four distinct regions exist in the diagram. The first colored in blue is a region with [111] easy direction where K_1 and K_2 are negative value. The second region colored in green, where K_1 is positive and $K_2 < -9K_1$, with [111] easy direction but also has a metastable [100] direction. Next, the yellow region, where K_1 is positive and $-9K_1 < K_2 < -2K_1$, which has a [100] easy direction with a [111] metastable direction. Finally, the red region, where $K_2 > -2K_1$, has a [100] easy direction.

response to changes in the anisotropy constants. This could be envisioned by crossing the green and yellow metastable regions at steeper angles increasing the temperature range in the two phase region.

The second type of scans were longer (~1hr) to gather data suitable for Rietveld refinement on TDF65. The 2θ angle was rotated from -6-$28°$ with a step size of $.001°$ and $.1$ sec/step which gives the detector coverage shown in Figure 3.2. Rietveld

refinement of the powder diffraction data was performed in GSAS using the EXPGUI (55; 56) software. The refinements were performed with profile function 3. The background was set to type 1 (Shifted Chebyschev polynomial) with 15 terms. The profile terms refined were LX, LY, shift, and ptec. Additional parameters refined included the unit cell, the occupancy of the rare earth site, and the thermal parameter U_{iso} for each site. The thermal parameter of all atoms of the same type and all atoms on the same site were initially fixed to be the same although this constraint was usually lifted by the end of the refinement. Also, when refining the occupancy of the rare earth site the Tb to Dy ratio was constrained to be the initial composition ratio.

TDF65 can be refined with a cubic symmetry, space group Fd-3m, at 100K, Figure 3.7(a). In TDF alloys the low temperature phase is isostructural with $NdCo_2$ (57) and thus tetragonal, however, even the phenomenal resolution of 11-BM wasn't sufficient to resolve the tetragonal distortion (47). At higher temperatures the refinement shows rhombohedral symmetry, space group R-3m, Figure 3.7(b). In the transition region there is a clear coexistence of two phases (tetragonal (cubic) + rhombohedral), Figure 3.7(c-f). Table 3.2 lists the lattice parameters, atom positions, and χ^2 for the cubic and rhombohedral phases. While refining two phases in the transition region it was noted that the Lorentzian strain broadening parameter increased dramatically through the transition region and the phase fraction of the rhombohedral began to climb. Taking a closer look at the fit of the characteristic 222 reflection at 160K, shown in Figure 3.8(a), the profile doesn't match the characteristics of the peak although the fit is of sufficient quality. Adding a second cubic phase, with a phase fraction ≈15%, the refinement improves substantially for the diffraction pattern taken at 160K, Figure 3.7 (f), and shown in Figure

3.8(b) is the characteristic 222 peak with a much closer fit and better match to the characteristic fit. The additional phase is highly distorted with a Lorentzian strain broadening parameter an order of magnitude higher than the other phases and relaxed the strain broadening parameters of the other two phases to levels closer to the parent phases. This indicates the region around the MPB has a large strain gradient. The second cubic phase could be thought of as a transition phase between the rhombohedral and tetragonal (cubic) parent phases in the MPB. This phase was also added in the 175K refinement with similar results although not shown. Finally, Table 3.3 displays the phase fractions and Lorentzian strain broadening terms for each phase in the transition region.

Figure 3.7: Calculated and experimental intensities of synchrotron powder diffraction in TDF65 for a) 100K, b) 295K, c) 185K.d) 180K, e) 175K, and f) 160K. Insets are enlargements of high angle data. Black crosses are measured data, red lines are calculated peaks, green is the background, and blue is the difference. In (a) Phase 1 indicates calculated Bragg reflections for cubic phase, in (b) Phase 2 indicates calculated rhombohedral peak positions, in (c), (d), and (e) Phase 1 indicates calculated cubic peak positions while Phase 2 indicates calculated rhombohedral peak positions, in (f) Phase 1 and Phase 4 indicate calculated cubic peak positions for each respective cubic phase and Phase 3 indicates calculated rhombohedral peak positions.

a)

TERFENOL650_100K cycle 474 Hist 1

b)

64

c)
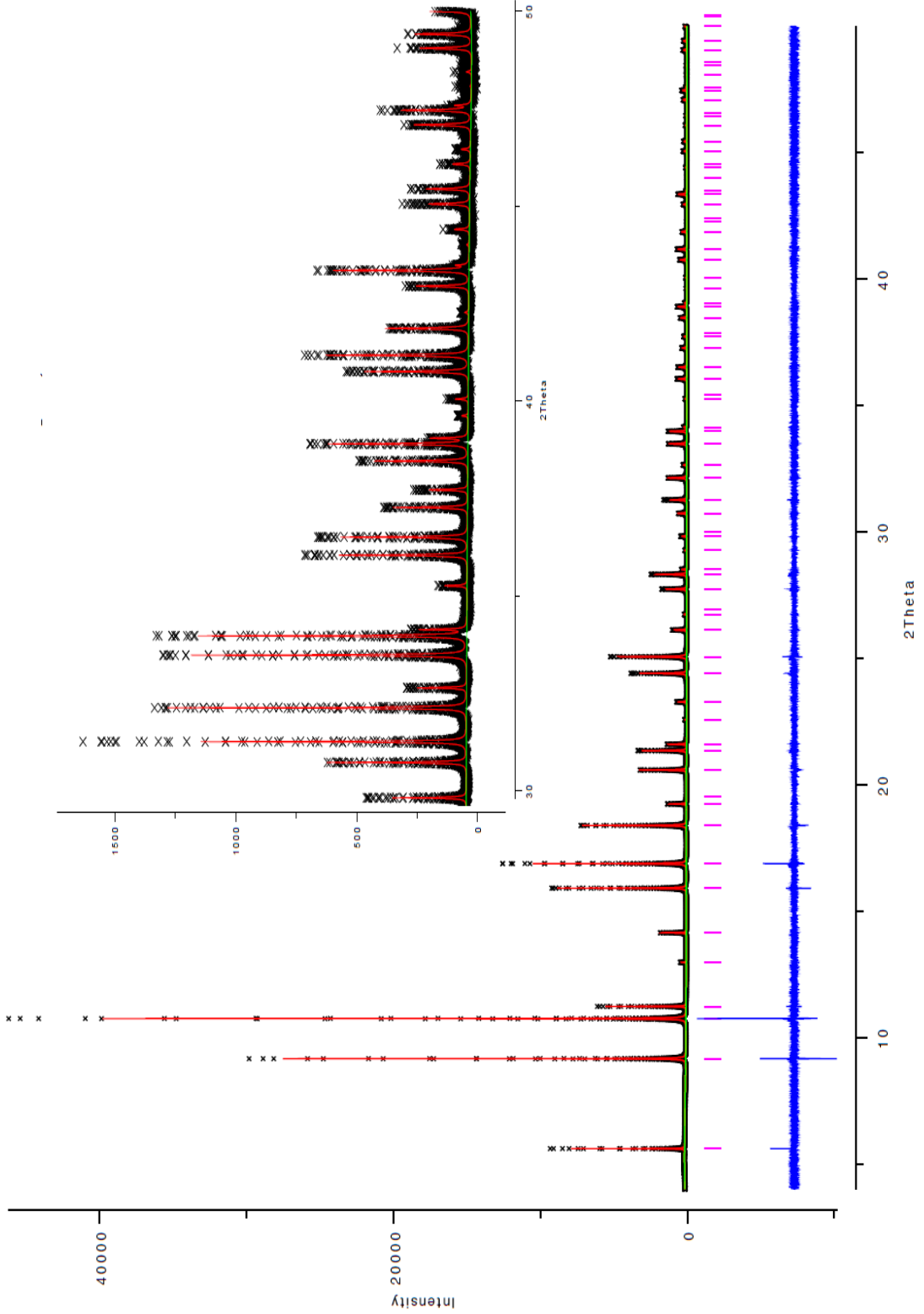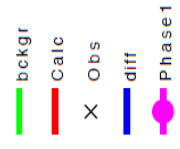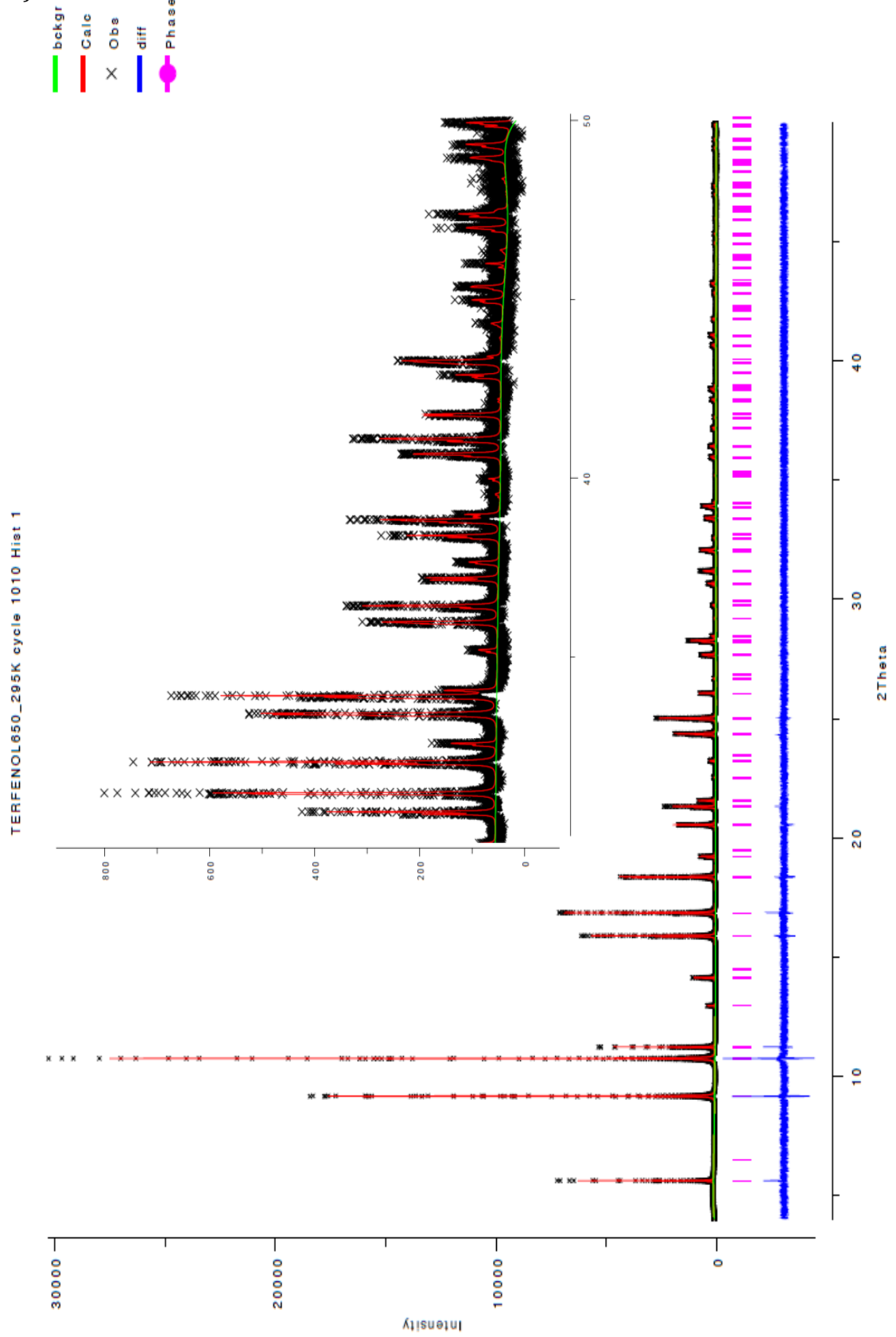
TERFENOL650_185K cycle 104 Hist 1

d)

bckgr
Calc
× Obs
diff
Phase1
Phase2

TERFENOL850_180K cycle 40 Hist 1

2Theta

Intensity

e)

	bckgr
	Calc
×	Obs
	diff
	Phase1
	Phase2
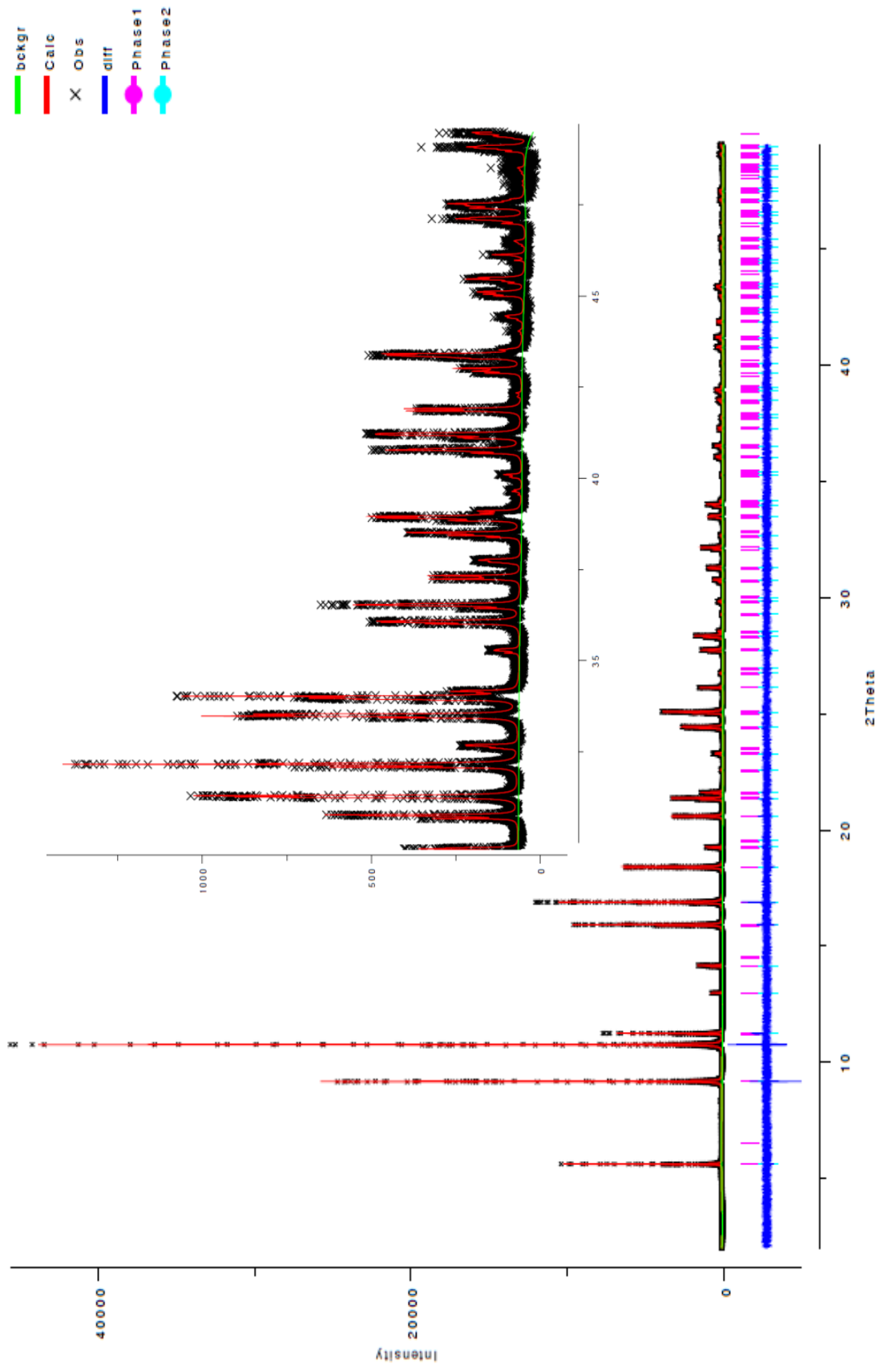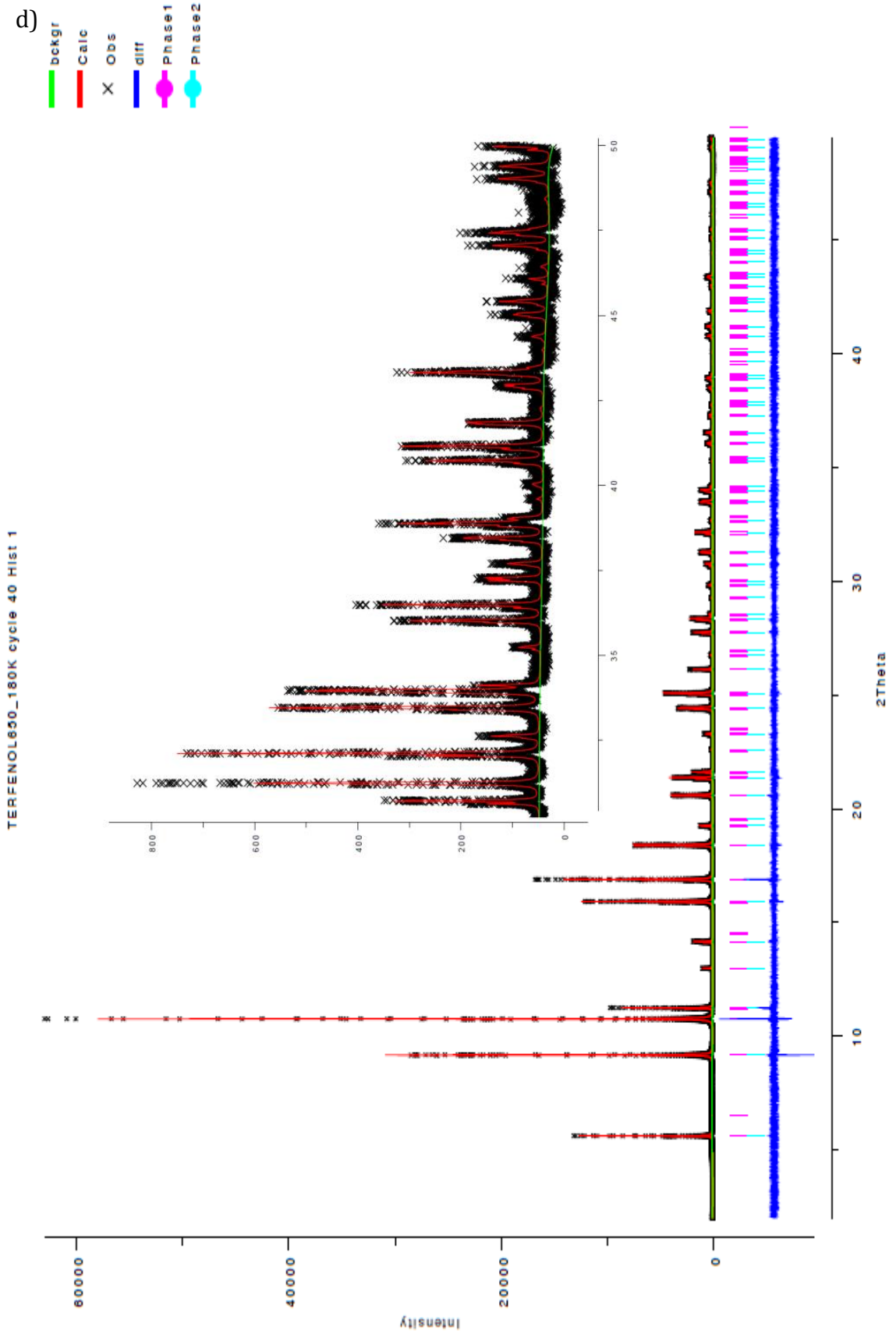
TERFENOL650_175K cycle 160 Hist 1

2Theta

Intensity

67

f)

bckgr
Calc
Obs
diff
Phase1
Phase3
Phase4

1R+2C_TERFENOL850_180K cycle 314 Hist 1

Intensity

2Theta

68
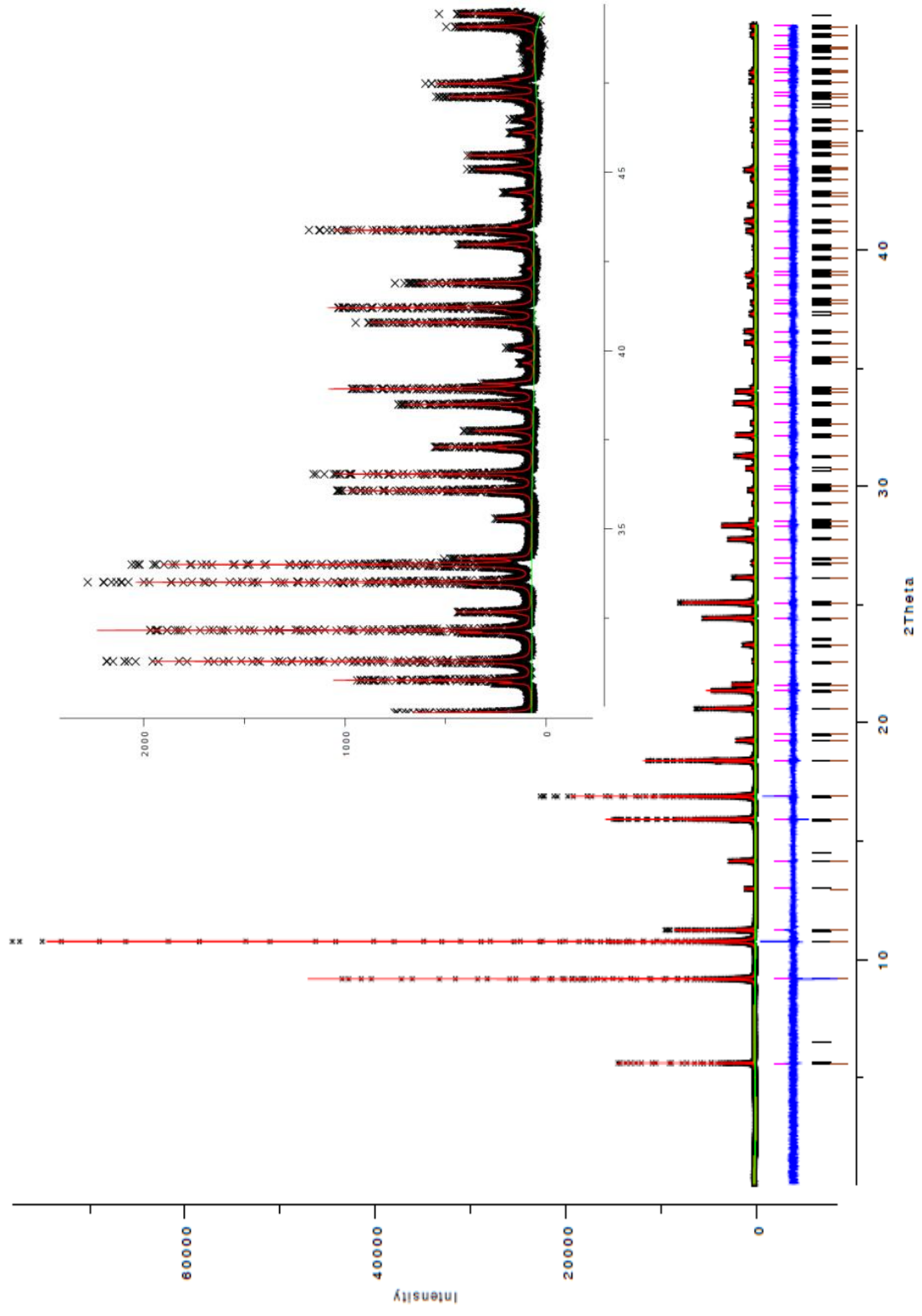
T (K)	100	295
a(Å), b(Å)	7.320307(7)	5.182988(6) 7.3299 (cubic equivalent)
c(Å)	7.320307(7)	12.727634(25) 7.3483 (cubic equivalent)
V(Å^3)	392.273(1)	296.100(1)
Atom	Tb 8a (1/8, 1/8, 1/8)	Tb 6c (0, 0, .125)
B(Å^2)	.271	.601
Atom	Dy 8a (1/8, 1/8, 1/8)	Dy 6c (0,0, .125)
B(Å^2)	.271	.601
Atom	Fe 16d (1/2 , 1/2, 1/2)	Fe 3b (1/2, 0, 0)
B(Å^2)	.198	.458
Atom		Fe 9e (0, 0, 1/2)
B(Å^2)		.356
wRp (Fitted)	.1279	.1250
wRp (-Bkgd)	.1336	.1283
χ^2	2.644	2.494

Table 3.2: Refined lattice and thermal parameters of TDF65 for the rhombohedral and cubic phases. χ2 values included to show accuracy of fit.

Figure 3.8: Plots of the refined 222 reflection for a) cubic and rhombohedral phases only and b) cubic and rhombohedral with a second cubic transition phase that is highly distorted.
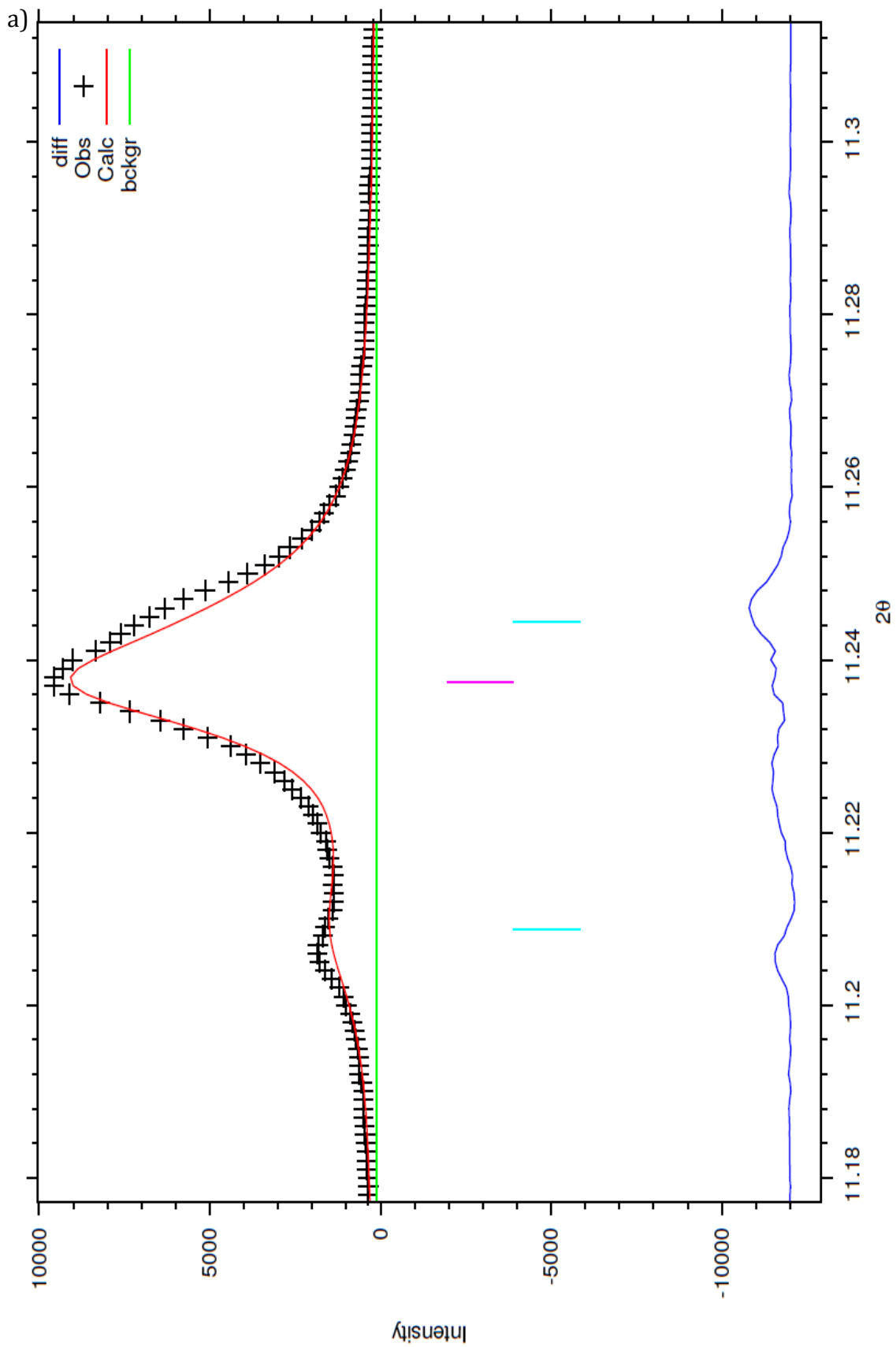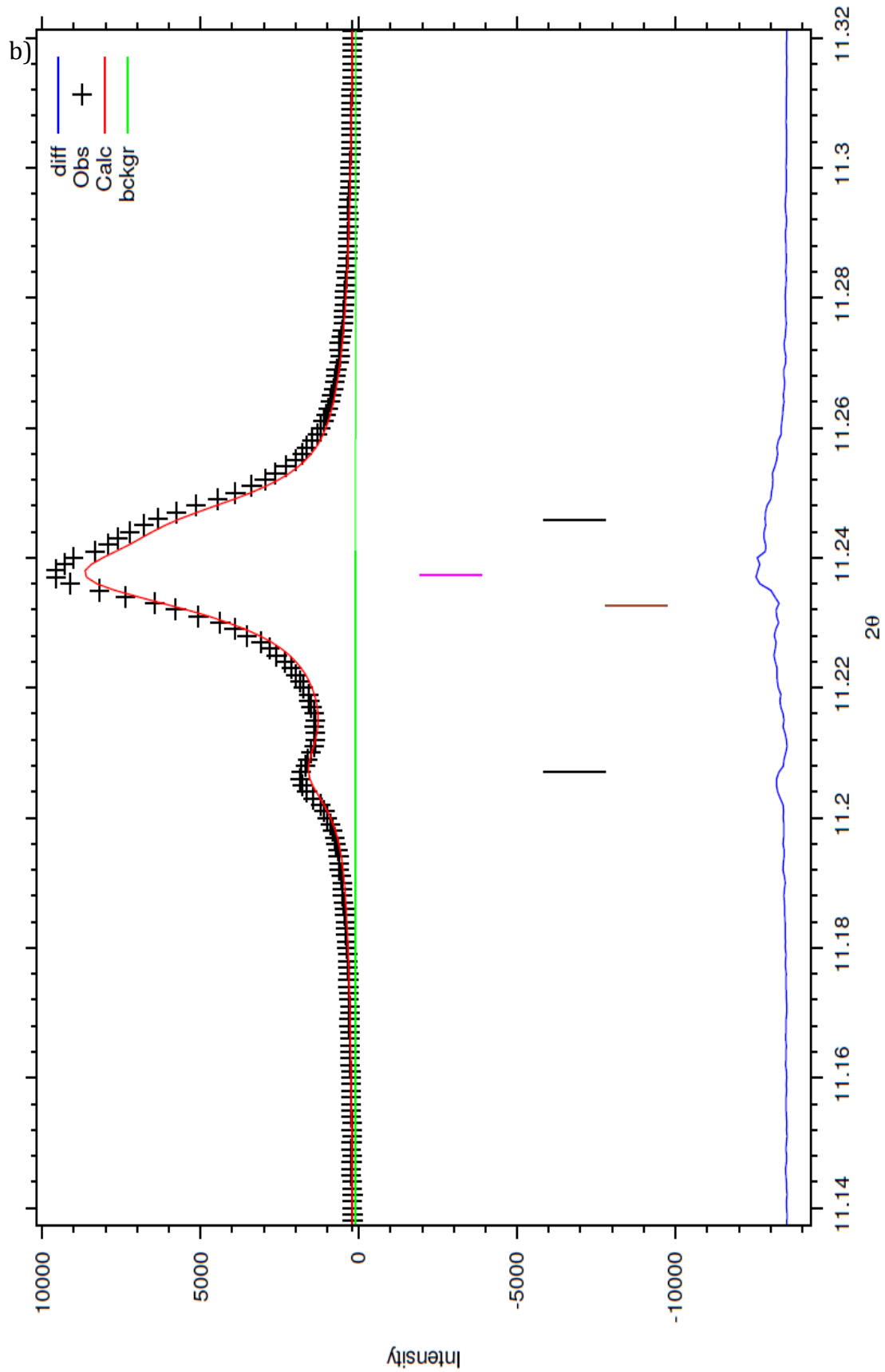
160K	Fraction	Avg crystallite Size (nm)	Strain (%)
Cubic	51.1%	1400	.128
Rhombohedral	31.1	1610	.11
Cubic 2	17.8	250	.758

175K	Fraction	Avg crystallite Size (nm)	Strain (%)
Cubic	51.1	380	.205
Rhombohedral	48.9	1280	.112

180K	Fraction	Avg crystallite Size (nm)	Strain (%)
Cubic	42.8	460	.282
Rhombohedral	57.2	1160	.091

185K	Fraction	Avg crystallite Size (nm)	Strain (%)
Cubic	36.1	400	.338
Rhombohedral	63.9	1340	.0876

Table 3.3: Phase fractions, average crystallite size, and strain percentage for TDF65 at various temperatures. Calculations for average crystallite size and strain percentage are $p = \frac{18000K\lambda}{\pi LX}$ and $S = \frac{\pi}{180}LY$ respectively. Note: Crystallite sizes over 200nm are large and only represent that the crystallite size doesn't contribute to peak broadening.

Chapter 4: Neutron Diffraction

4.1   Overview

X-ray and synchrotron X-ray diffraction were performed to elucidate the nature of the structural transformation as temperature and composition of the TDF alloys is varied. While these techniques provided a sufficient structural model of the phase transition details about the magnetic moments or directions at the phase transition cannot be extracted from X-ray diffraction. Therefore, temperature dependent neutron powder diffraction patterns were taken to investigate the magnetic structure of TDF alloys with the presence of MPB regions. Neutron diffraction patterns were taken at various temperatures above, below, and inside the region where the MPBs exist.

4.2   Background

Neutron diffraction is a technique that uses the neutron as a diffracting probe instead of the EM radiation in X-ray diffraction. While the basic principles of neutron and x-ray diffraction are the same the patterns produced by each can be quite different. X-rays are a form of EM radiation therefore they interact with the electron cloud. The X-ray scattering amplitude is proportional to the atomic number, Z, represented mathematically by

$$ZA\frac{e^2}{mc^2}\frac{1}{r} \tag{4.1}$$

where A is the amplitude of the electric field, e is the charge of an electron, m is the rest mass of an electron, c is the speed of light, and r is the distance of the observation. The X-ray is a form of electromagnetic radiation therefore they interact with the electron

cloud, which is on the order of the X-ray wavelength, so an atom's form factor decreases as

$$f \propto \frac{\sin \theta}{\lambda} \tag{4.2}$$

Neutrons are scattered by two different mechanisms nuclear and magnetic. Since neutrons are particles they scatter off of the nuclei. Neutrons have wildly varying scattering cross sections for each element and even isotopes so they provide information that is complimentary to X-rays Fig 4.1. Neutrons are especially sensitive to light elements making neutron diffraction the method of choice for those studying soft matter. The dimensions of the nucleus are significantly smaller than the wavelength of the neutrons so the form factor of an atom in neutron scattering is independent of scattering angle.
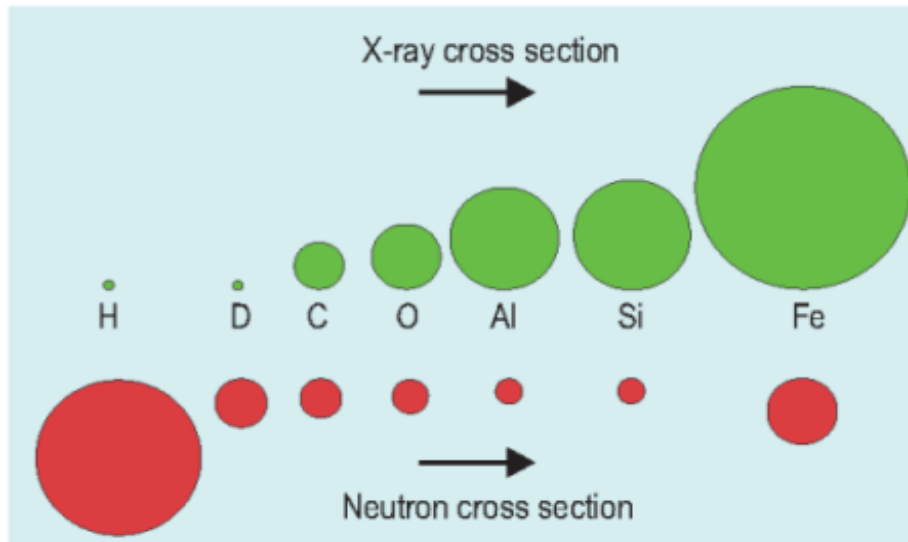
Fig 4.1: Comparison of neutron and X-ray scattering cross sections (66).

4.2.1   Neutron Diffraction

For a comprehensive analysis of neutron diffraction the reader is referred to the many texts available on the subject, especially (58; 59). Neutrons are subatomic particles with a rest mass of 1.67 x 10^{-24}g that possess zero charge and a magnetic moment of 1.04 x $10^{-3}\mu_B$. Since the neutrons are moving particles they have an associated wavelength, λ, given by the de Broglie equation

$$\lambda = \frac{h}{mv},\tag{4.3}$$

where h is Plank's constant and v is the neutron velocity. Neutrons have no internal long range forces so there is no potential energy between them. They can be thought of as a gas and therefore a temperature can be derived from their velocity

$$E = \frac{mv^2}{2} = \frac{3kT}{2}.\tag{4.4}$$

Substituting back into Eq 4.3 we obtain

$$\lambda^2 = \frac{h^2}{3mkT}.\tag{4.5}$$

From Eq 4.5 it can be shown that thermal neutrons at 300K have a wavelength of 1.45Å. This is quite fortunate because the spacing between atomic planes is of the same order as the wavelength of the thermal neutrons.

If we have a plane wave of neutrons incident on a nucleus centered at the origin represented by the wave-function

$$\Psi = e^{ikz},\tag{4.6}$$

the scattered wave will have spherical symmetry since the nucleus acts as a point scattering center. The wave-function representing the scattered wave will be of the form

$$\Psi = -\frac{b}{r}e^{ikr},\tag{4.7}$$

with r being the distance from the origin to the point of observation and b is the scattering

length. The resulting neutron wave will be described by

$$\Psi = e^{ikz} - \frac{b}{r} e^{ikr}. \tag{4.8}$$

The nucleus has a scattering cross section defined by

$$\sigma = 4\pi r^2 v \frac{\left|\frac{b}{r} e^{ikr}\right|^2}{v\left|e^{ikz}\right|^2} = 4\pi b^2, \tag{4.9}$$

with v the neutron velocity.

Neutrons are not only scattered by the nucleus. They possess a magnetic moment

and as such they are also scattered by the magnetic lattice in magnetic materials. The

magnetic scattering provides a probe to investigate the magnetic structure of the crystal

and the magnetic moments of magnetic atoms. To separate the nuclear and magnetic

scattering we must look at the form factors. The nucleus can be thought of as a point

scattering center so the form factor of nuclear scattering is independent of the scattering

angle. Magnetic scattering takes place in the outer electron shells so the form factor for

magnetic scattering falls off quickly with increasing angle due to interference effects

from the scattering taking place at various positions in the atom.

The magnetic differential scattering cross section for neutrons is given by the

relation

$$d\sigma_m = q^2 S^2 \left(\frac{e^2 \gamma}{mc^2}\right)^2 f^2, \tag{4.10}$$

where γ is the neutron magnetic moment, S is the number of unpaired spins, and f is the

magnetic form factor. The magnetic interaction vector, q, can be represented as

$$q = \varepsilon(\varepsilon \cdot K) - K, \tag{4.11}$$

where K is a unit vector in the direction of the atomic magnetic spin and ε is the scattering vector. The total differential scattering cross section is then the sum of nuclear and magnetic contributions given by

$$d\sigma = b^2 + 2bp(\lambda \cdot q) + p^2 q^2,$$ (4.12)

where λ is a unit vector representing the direction of spin in the incident neutron and p is represented as

$$p = \left(\frac{e^2 \gamma}{mc^2}\right) Sf.$$ (4.13)

For unpolarized neutrons λ takes all possible orientations, consequently, the center term drops out of Eq 4.12 and we obtain

$$d\sigma = b^2 + p^2 q^2.$$ (4.14)

4.2.2   Time-of-Flight Neutron Diffraction

In time-of-flight (TOF) neutron diffraction the sample is exposed to an incident beam of neutrons from pulsed source. Neutrons of different wavelengths will travel different speeds from the chopper to the sample. In this case the detector is set at a fixed angle 2θ from the sample and collects all or a portion of the halo from the Debye-Scherrer cone as a function of time. From Eq 4.3 we know that neutrons wavelength is related to their velocity. The velocity can be measured as a function of the time of flight and the length of the flight path from chopper to detector as

$$v = \frac{L}{t}.$$ (4.15)

The resolution of the instrument can be defined by

$$\frac{\Delta\lambda}{\lambda} = \frac{\Delta t}{t} = \frac{\Delta t}{L}\frac{h}{m\lambda} = \frac{\Delta t}{L}\frac{h}{2md\sin\theta},$$ (4.16)

where the highest resolution is achieved for large values of the interplanar spacing. The integrated reflection, R^λ, for white radiation is given by

$$R^\lambda = R^\theta \lambda \cot \theta. \tag{4.17}$$

Given a cylindrical powder sample the number of neutrons per minute incident on the counter is

$$P = i(\lambda) \frac{\lambda^3 l_s}{8\pi r} \frac{V p'}{p} \frac{j N_c^2 F^2}{\sin \theta \sin 2\theta} \lambda \cot \theta \, e^{-2W} A_{hkl}, \tag{4.18}$$

where l_s is the height of the counter slit, r is the distance from the sample to the counter, V is the volume of the sample, j is the number of planes for the particular reflection being counted, p and p′ are the measured and theoretical densities respectively, e^{-2W} is the Debye temperature factor, N_c is the number of unit cells per cm^3, F is the form factor of the unit cell, A_{hkl} is the adsorption factor, and $i(\lambda)d\lambda$ is the flux of neutrons between λ and $\lambda+\Delta\lambda$ (58).

4.3 POWGEN

The Spallation Neutron Source (SNS) at Oak Ridge National Laboratory (ORNL) provides the most intense pulsed neutron beams in the world (60). Neutrons are produced through a process known as spallation where microsecond pulses of protons are
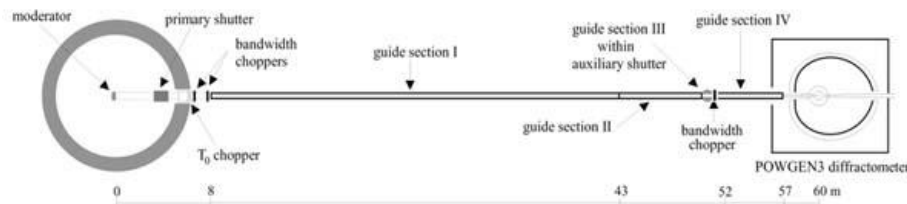

Figure 4.2: Beamline schematic of the POWGEN powder diffractometer at SNS (61).

accelerated at a heavy metal target with high velocity and upon impact expel neutrons. The expelled neutrons are moderated to thermal velocities for diffraction. POWGEN is a third generation time of flight neutron diffraction instrument set up 60m from the target Figure 4.2 (61). For a complete description of the instrument the reader is referred to the above reference. The third generation design allows wide and continuous data collection from the user chosen bank. This allows datasets from different banks to be merged into a single refinement. There is a series of three bandwidth choppers located at 6.65, 7.90 and 49.98m designed to set the incident wavelength bandwidth and prevent frame overlap, where fast neutrons from the next pulse overlap slow neutrons from the current pulse. POWGEN is equipped with the FERNS automated sample changer which provides sample environments from 20-300K and allows rapid sample changing while at low temperatures.

TDF powders were loaded into vanadium cans with a diameter of 8mm and a specimen weight of ~4g per can and neutron powder diffraction patterns were taken at room temperature. Patterns of TDF65 were taken at 100K, 300K, and 160-195K in 5K steps. Scans were taken at wavelength 2 (1.066Å) and 6 (3.73Å) for each temperature. The data were refined with the FullProf software (62). These refinements were substantially affected by Dy absorption so care was taken to avoid unreasonable values for parameters that could correlate with absorption. The absorption on the lower wavelength band proved too difficult to refine since the powder patterns only consist of five peaks so they were omitted from the refinement.

4.4   Results

Refinement of all patterns was performed in a cubic symmetry as the resolution wasn't sufficient to detect the peak splitting in neither the rhombohedral nor the tetragonal symmetry regions. After the nuclear contribution was refined in the F d -3 m space group the magnetic contribution to the diffraction pattern was refined in the F-1 space group. Graphing the thermal parameters of the TDF65 sample as a function of temperature, Figure 4.3, indicates a phase change occurring below 180K. The temperature region of the phase change is comparable with the data from the synchrotron diffraction. Magnetic moments were refined for the rare earth and Fe sites independently.
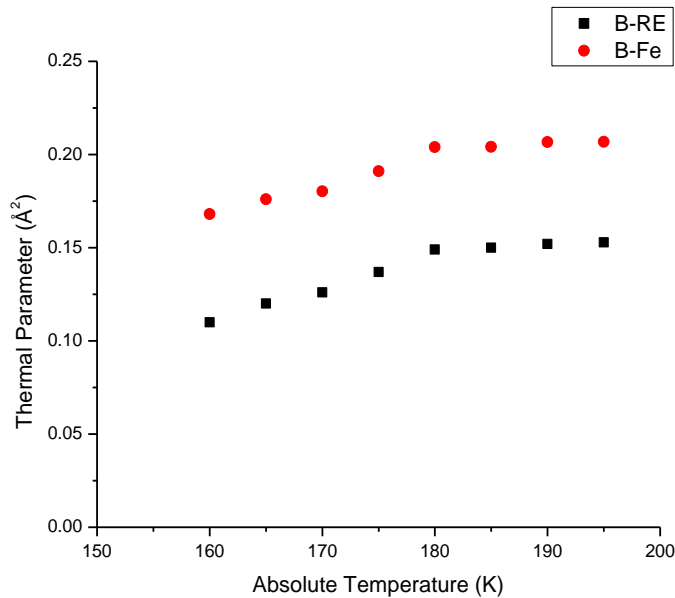
Figure 4.3: Refined thermal parameters for TDF65 alloys. Large slope at lower temperatures is indicative of a phase change.

The rare earth sites were refined using one Tb moment occupying all of the rare earth sites instead of separate Tb and Dy moments occupying fractions of the rare earth sites since the software requires many constraints in order to successfully refine the RE sites independently. The temperature dependence of the moments is displayed in Figure 4.4.

The moments for both the rare earth (~9μ_B) and the Fe (~-2μ_B) sites are invariant within experimental error over the temperature range measured. The refinement of TDF65 at 175K is shown in Figure 4.5
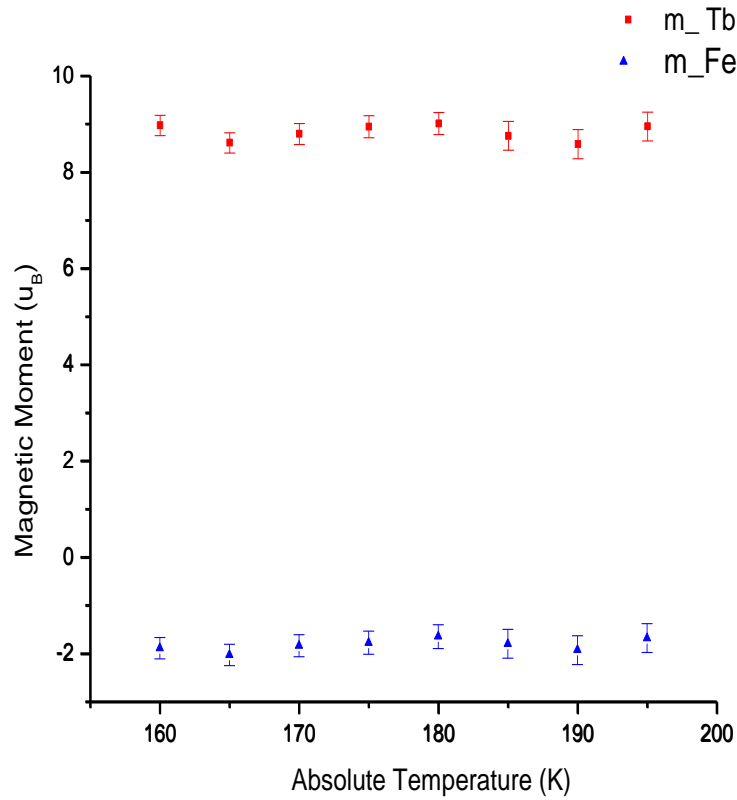
Fig 4.4: Refined magnetic moments for the rare earth and iron sites at various temperatures in the transition region.

Figure 4.5: a) Refinement of POWGEN data for TDF65 taken at 175K. b) Enlargement of short TOF data.

a)

160K Quick Scan

b)

160K Quick Scan

t.o.f. (μ *sec.*)

Intensity (arb. units)
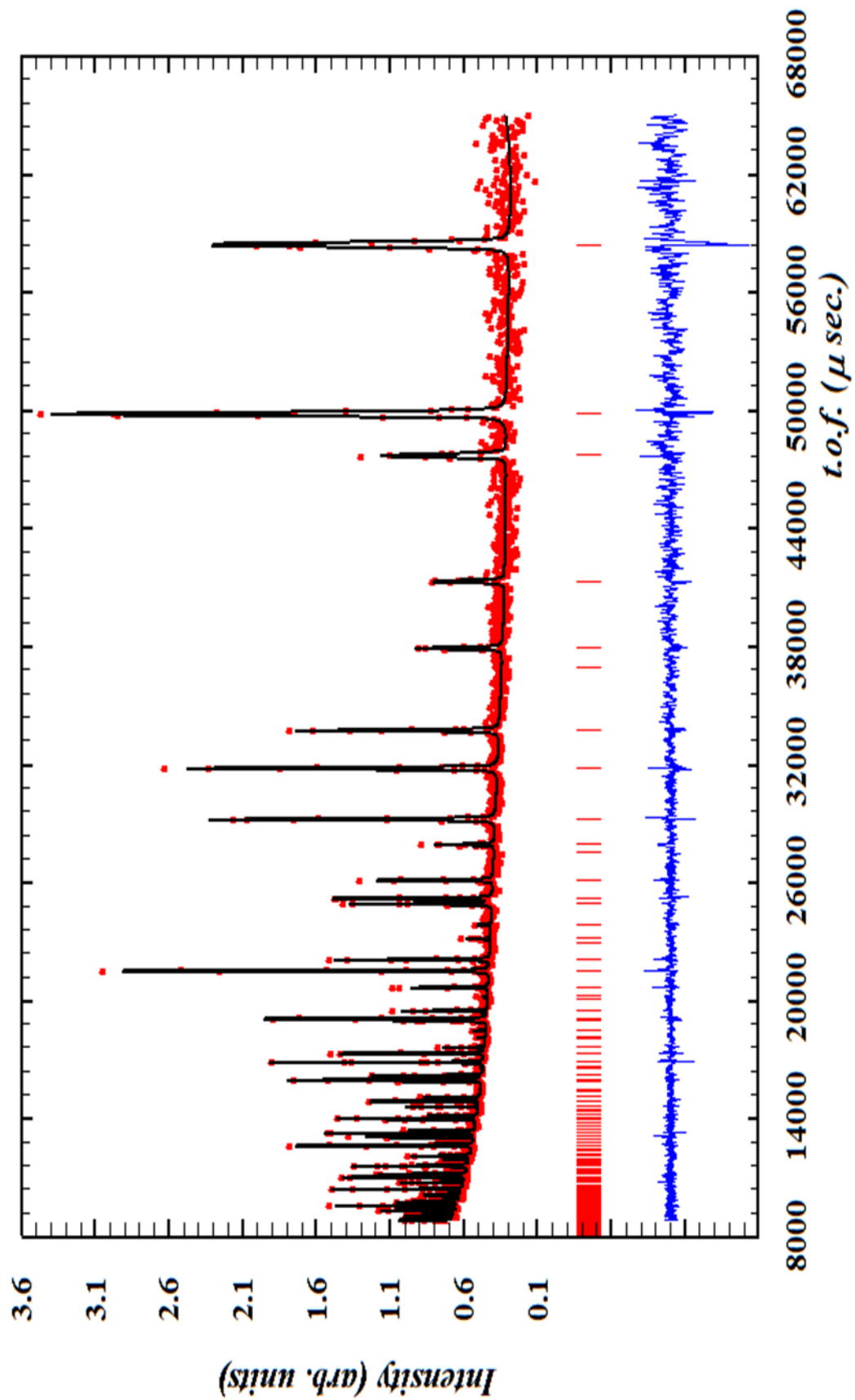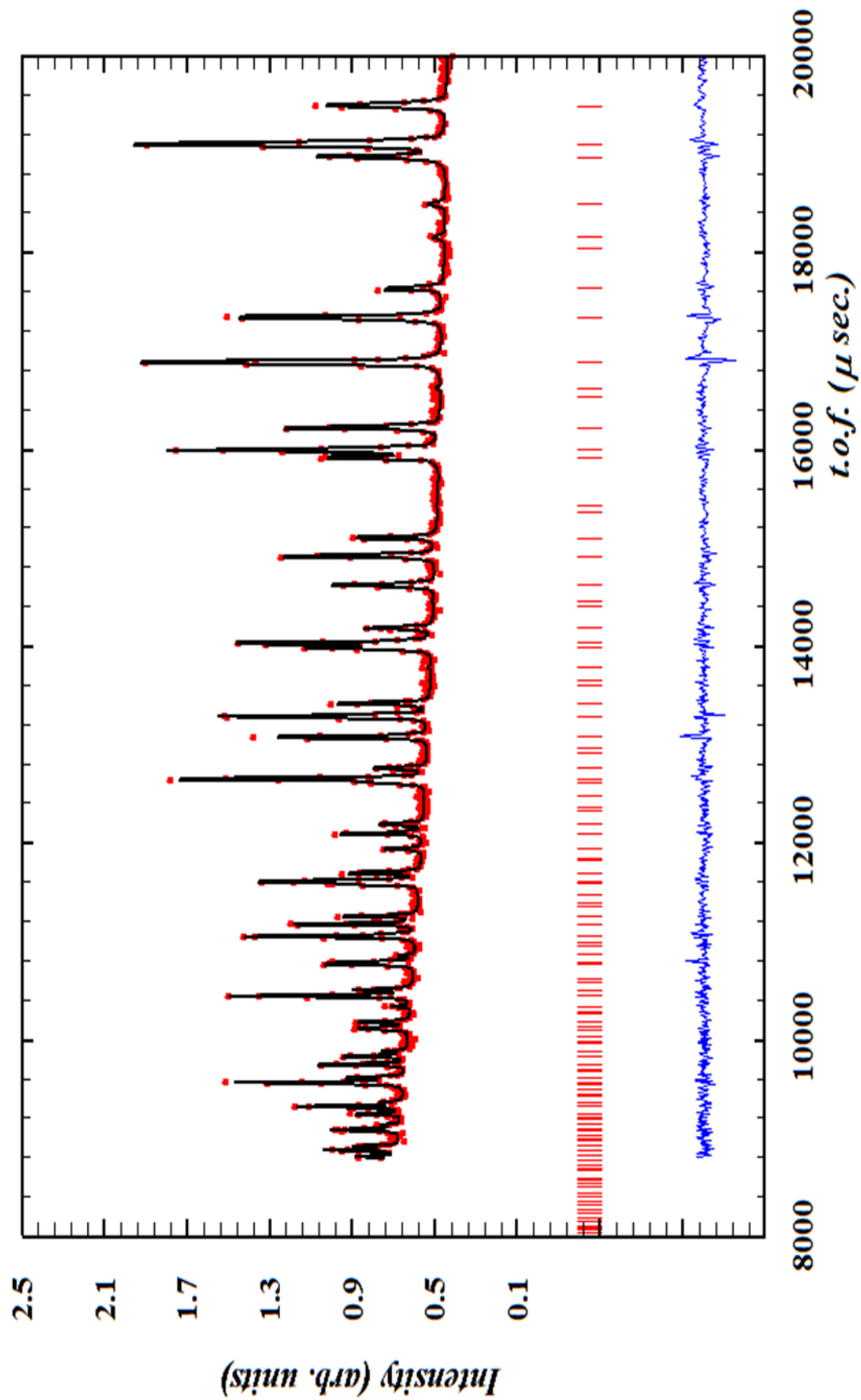
4.5   Conclusions

While the neutron diffraction data from POWGEN didn't provide all details we were interested in investigating they did elucidate useful characteristics of MPB. In TDF65 we can clearly see that the thermal parameter of the Fe and RE sites changes slope at 180K indicating the phase change is completed. The main result of interest is that the magnetic moments of the Fe and RE sites are invariant within experimental error throughout this transition region. This indicates that the magnetic direction is either rotating from the [100] to the [111] direction or is made up of small discrete domains whose direction is influenced by the local concentration of REs (63).

Chapter 5: Summary, Contributions, and Future Research

Morphotropic phase boundaries in ferroelectrics have been the source of countless investigations since increased values of the response coefficients in PZT were first reported by Jaffe (4). Two competing theories explaining the observed lower symmetry phases present at the MPB have been forwarded. The first theory pertains to local monoclinic supercells that form along the MPB region. In the second theory meso-structures form composed of nanotwins of orientation variants of the parent phase. These meso-structures explain the intrinsic relationships between the parent phase and the monoclinic like phase.

The first report of MPBs in ferromagnets has only recently been presented in the $Tb_{1-x}Dy_xCo_2$ system (9). Unfortunately, the Curie temperature of this system is $\approx200K$ so the authors were unable to determine the MPB properties of ferromagnets at high temperature. Since ferromagnets share many physical parallels with ferroelectrics it may be tempting to consider the research on the MPB region of ferroelectrics directly applicable to ferromagnets. However, in ferroelectrics the ferroic order and the local atomic displacements cannot be separated due to their rigid structure. In contrast, the ferroic order in ferromagnets is governed by the compromise between the anisotropy and the exchange energies. While the exchange energy is temperature independent the magnetocrystalline anisotropy is highly temperature dependent. This thesis provides insight into the changing nature of the structure of MPBs in TDF alloys at higher temperatures brought about by changes in magnetocrystalline anisotropy constants with temperature.

5.1   Summary of Research

TDF alloys were investigated with several macroscopic and microscopic techniques. In chapter 2 macroscopic characterization methods including M(H), M(T), λ(H,T) were described. M(H) and M(T) data taken from the VSM provided initial confirmation of sample quality and established T_C=670K for TDF65. The SQUID magnetometer was utilized to take M(T) data at low temperatures with an applied field of 100Oe. The magnetic transition from [100] to [111] easy direction was easily seen as a maximum in the M(T) curves. The maxima for each TDF alloy broadened with increasing concentration of $DyFe_2$. This broadening is attributed to the increasing width of the two phase MPB region with increasing temperature. The magnetostriction, λ(H), of various TDF alloys was measured at room temperature and at 25C increments up to 200C. Values of magnetostriction in TDF72.5 of ~1600$\mu\varepsilon$ were measured which is equivalent to previously reported values at room temperature. In alloys with higher $DyFe_2$ concentrations (TDF75-TDF80) the expected transition temperature is above RT. Therefore, in these alloys as the temperature is increased the magnetostrictive susceptibility increases to a maximum value at the temperature of the magnetic transition. This change in magnetostrictive susceptibility establishes that the boundary between the tetragonal and rhombohedral states is magnetoelastic in nature. A preliminary phase diagram was made identifying the phase transition temperature as the maxima in the magnetic susceptibility. This proved useful in identifying the temperature region of interest in the synchrotron and neutron diffraction measurements reported in chapter 3 and chapter 4.

In chapters 3 and 4 the microscopic characteristics of the TDF alloys were probed with temperature dependent synchrotron and neutron diffraction. Parametric powder patterns were taken as the temperature was constantly ramped in several TDF alloys. The profile fitting of the 440 cubic peak exhibits a clear two phase region that is widening in its temperature range as $DyFe_2$ composition is increased. The two phase region is expected from a first order transition with accompanying MPBs and agrees with previous reports on the similar $Tb_{1-x}Dy_xCo_2$ system. The widening of the two phase region with increasing $DyFe_2$ composition indicates that domains oriented in the [111] direction are meta-stable for a wider temperature range. This result was unexpected but can be readily interpreted by the temperature dependence of the magnetocrystalline anisotropy. A consequence of this structural analysis separates the low temperature "spin transition region," where higher order anisotropy terms allow a rotation of the magnetization, from the high temperature MPB region.

High resolution powder diffraction patterns were taken on TDF65 at temperatures above, at MPB temperatures, and below the transition region. At low temperatures the structure is cubic, with Fd-3m symmetry, and at high temperatures the structure is rhombohedral, with R-3m symmetry. In the transition region a second cubic phase with ≈15% phase fraction was added to produce a satisfactory refinement. This cubic phase is highly strained as evidenced by the large value for the Lorentzian strain broadening parameter, LY, in the refinement. Adding this additional phase relaxed the other two phases in the refinement which indicates that there is a large strain gradient across the MPB with strains returning to normal inside of each domain. This second cubic phase can

be thought of as a transition phase between the parent tetragonal (cubic) and rhombohedral phases.

Neutron diffraction patterns were taken with the intent of observing the magnetic moment and the magnetic direction through the transition region in TDF65. The resolution of the POWGEN instrument wasn't sufficient to resolve the rhombohedral distortion so the magnetic direction couldn't be identified in the refinement. The magnetic moments of both the RE and the Fe site remained invariant throughout the transition region indicating that the magnetic transition from [100] to [111] has two possible mechanisms. The first mechanism is a rotation of the entire magnetic moment from [100] to the [111] direction. The second mechanism, which is supported by our synchrotron diffraction results, consists of nanodomains forming with [111] magnetization in Tb rich areas of the solid solution. The number of these domains would grow in population as temperature is increased producing a rotation of the combined magnetization.

5.2   Contributions of this Research

In this thesis the fundamental difference between the MPB in ferroelectrics and ferromagnets has been investigated and clarified. Since the mechanism behind the ferroic order in ferroelectrics and ferromagnets differs one would expect the phase transition in each to behave differently. It has been shown that in TDF alloys a clear widening of the two phase region occurs at elevated temperatures. This is explained by the change in the magnetocrystalline anisotropy terms as a function of temperature, described in Eq 1.4. While neutron diffraction results were not as clear as we hoped they did provide

interesting information about the invariance of the magnetic moments in the phase transition region.

5.3   Future Research

While TDF alloys have already been studied in great detail, one could envision several future experiments derived from this research. The most logical follow up experiment would be to obtain TDF alloys with higher $DyFe_2$ concentrations and finish mapping out the high temperature MPB region to see if it intersects with T_C as expected or if some interesting phenomena, such as a change to a second order transition, occurs. It would be interesting to compare the field cooled and zero field cooled M(T) data with that from an AC magnetic susceptibility measurement. This could provide more insight into the broadening of the maxima in the M(T) curves. A second experiment that would be interesting would be to analyze the change in lattice parameters of TDF alloys under an applied field to investigate if they are constrained to the same invariance conditions that are found in ferroelectrics (6; 28). The final experiment that could be proposed would be to return to POWGEN, if sufficient beamtime could be awarded, and design the experiment for maximum resolution by trading for increased count times for each temperature to investigate the magnetic directions in the phase transition region.

Bibliography

1. **Clark, A.E.** *Highly Magnetostrictive Rare Earth Alloys.* Silver Spring, MD : Naval Surface Weapons Center Technical Report, 1976.

2. Terfenol-D. *Etrema Products, Inc.* [Online] [Cited: December 5, 2012.] Etrema Products, Inc..

3. **Callister Jr., W.D.** *Materials Science and Engineering an Introduction.* New York, NY : John Wiley & Sons, Inc., 2000. p. 247.

4. **Jaffe, B., Roth, R.S. and Marzullo, S.** 1954, J. Appl. Phys., Vol. 25, p. 809.

5. **Atzmony, U and Dariel, M.P.** 9, s.l. : Physical Review B, 1973, Vol. 7, p. 4220.

6. **Jin, Y.M., Khachaturyan, A.G. and Viehland, D.** 19, 2003, Physical Review Letters, Vol. 91, p. 197601.

7. **Ahart, M., Somayazulu, M. and Cohen, R.E.** 2007, Nature, Vol. 451, p. 545.

8. **Liu, W. and Ren, X.** 257602, 2009, Physical Review Letters, Vol. 103.

9. **Yang, S., Bao, H. and Ren, X.** 2010, Physical Review Letters, Vol. 104, p. 197201.

10. **Khachin, V.N., et al.** 3, 1987, Doklady Akademii nauk SSSR, Vol. 295, pp. 606-609.

11. **Spaldin, N.A.** [ed.] K. Rabe, C.H. Ahn and J.-M. Triscone. *Physics of Ferroelectrics.* 2007, Vol. 105, pp. 175-218.

12. **Wang, K.F., Liu, J.M. and Ren, Z.F.** 4, s.l. : Advances in Physics, 2009, Vol. 58, pp. 321-448.

13. **Kitagawa, Y., et al.** 2010, Nature Materials, Vol. 9, p. 797.

14. **Wang, J., et al.** s.l. : Science, 2003, Vol. 299, p. 1719.

15. **Ren, S., Briber, R. and Wuttig, M.** 17, s.l. : Applied Physics Letters, 2008, Vol. 93, p. 173507.

16. **Ren, S., Laver, M. and Wuttig, M.** 15, s.l. : Applied Physics Letters, 2009, Vol. 95, p. 153504.

17. **Kittel, Charles.** *Introduction to Solid State Physics.* s.l. : John Wiley & Sons, 2005. Vol. 8. 0-471-41526-X.

18. **Dong, X.L. and Kojima, S.** 11, 1997, J. Phys.: Condens. Matter, Vol. 9, p. L171.

19. **Chikazumi, S.** *Physics of Ferromagnetism.* Oxford : Clarendon Press, 1997.

20. **Heisenberg, W.** 9-10, s.l. : Zeitschrift für Physik A Hadrons and Nuclei, 1928, Vol. 49, p. 619.

21. **Shull, C.G., Strauser, W.A. and Wollan, E.O.** 1951, Physical Review, Vol. 83, p. 333.

22. **Otsuka, K. and Wayman, C.M.** *Shape Memory Materials.* New York, NY : Cambridge University Press, 1998. 0521663849.

23. **Noheda, B., et al.** s.l. : Applied Physics Letters, 1999, Vol. 74, p. 2059.

24. **Ehmke, M.C, et al.** 2012, J. Appl. Phys., Vol. 111, p. 124110.

25. **Rossetti, G.A. and Khachaturyan, A.G.** 11, s.l. : Journal of Applied Physics, 2008, Vol. 103, p. 114113.

26. **Atzmony, U, Dariel, M.P. and Dublon, G.** 7, s.l. : Physical Review B, 1977, Vol. 15, p. 3565.

27. **Noheda, B., et al.** s.l. : Physical Review B, 2000, Vol. 61, p. 8687.

28. **Wang, Y.U.** 2006, Physical Review B., Vol. 73, p. 014113.

29. **Wang, Yu U.** s.l. : Physical Reveiw B, 2007, Vol. 76, p. 024108.

30. **Khachaturyan, A.G.** 13, 1991, Physical Review B, Vol. 43, p. 10832.

31. **Schonau, K. and al., et.** s.l. : Physical Review B, 2007, Vol. 75, p. 184117.

32. **Alstad, J., Legvold, S. and Rhyne, J.** 1963, Physical Review Letters, Vol. 10, p. 509.

33. **Clark, A.E. and Benson, H.** 1972, Physical Review B, Vol. 5, p. 3642.

34. **Williams, C.M. and Koon, N.C.** s.l. : Journal de Physique, 1979, Vol. 40, p. 194.

35. Technical Specifications. *Lakeshore.* [Online] [Cited: December 17, 2012.] http://www.lakeshore.com/products/vibrating-sample-magnetometer/models/Pages/Specifications.aspx.

36. **McElfresh, M.** Application Notes. *Quantum Design.* [Online] [Cited: December 18, 2012.] http://www.qdusa.com/sitedocs/appNotes/mpms/FundPrimer.pdf.

37. Magnetic Property Measurement System. *Quantum Design.* [Online] [Cited: December 18, 2012.] http://www.qdusa.com/products/mpms.html.

38. **Newnham, R.E.** 1998, Acta Cryst, Vol. A54, p. 729.

39. **Palit, M., Pandian, S. and Chattopadhyay, K.** 2012, Journal of Alloy and Compounds, Vol. 541, p. 297.

40. *NobelPrize.org.* [Online] Nobel Foundation. [Cited: September 27, 2012.] http://www.nobelprize.org/nobel_prizes/physics/laureates/1901/.

41. **Warren, B.E.** *X-ray Diffraction.* Mineola, NY : Dover Publishing, 1990. 0-486-66317-5.

42. **Als-Nielsen, J. and McMorrow, D.** *Elements of Modern X-ray Physics.* s.l. : John Wiley & Sons, Ltd., 2001.

43. **Cullity, B.D.** *Elements of X-ray Diffraction.* s.l. : Addison-Wesley, 1978.

44. **Pecharsky, V.K. and Zavalij, P.Y.** *Fundamentals of Powder Diffraction and Structural Characterization of Materials.* New York, NY : Springer Science+Business Media, 2009. 978-0-387-09578-3.

45. **Rietveld, HM.** s.l. : Journal of Applied Crystallography, Vol. 2, p. 67.

46. **Thompson, P., Cox, D.E. and Hastings, J.B.** s.l. : J. Appl. Cryst., 1987, Vol. 20, p. 79.

47. **Yang, S. and Ren, X.B.** s.l. : Phys. Rev. B., 2008, Vol. 77, p. 014407.

48. 11-BM Frequently Asked Questions. *Advanced Photon Source Beamline 11-BM.* [Online] 2012. http://11bm.xor.aps.anl.gov/faq.html.

49. **Wang, J.** s.l. : Review of Scientific Instruments, 2008, Vol. 79, p. 085105.

50. **Staff, 11-BM.** Publishing 11-BM Results. *Argonne National Laboratory.* [Online] http://11bm.xor.aps.anl.gov/users_publish.html#describe.

51. *WinPLOTR: a Windows tool for powder diffraction patterns analysis.* **Roisnel, T. and Rodriguez-Carvajal, J.** s.l. : Materials Science Forum,Proceedings of the Seventh European Powder Diffraction Conference (EPDIC 7), 2000. p. 118.

52. **Callen, E. and Callen, H.B.** 1965, Phys. Rev., Vol. 139, p. A455.

53. **Callen, H.B. and Callen, E.** 1966, J. Phys. Chem. Solids, Vol. 27, p. 1271.

54. **Martin, K.N., et al.** 2006, J. Phys. Condens. Matter, Vol. 18, p. 459.

55. **Toby, B.H.** 2001, J. Appl. Crystallogr., Vol. 34, p. 210.

56. *General Structure Analysis System (GSAS).* **Larson, A.C. and Von Dreele, R.B.** 1994, Los Alamos National Laboratory Report, Vol. LAUR 86, p. 748.

57. **Xiao, Y.G., et al.** s.l. : J. Alloys Compounds, 2006, Vol. 420, p. 29.

58. **Bacon, G.E.** *Neutron Diffraction.* 3rd Ed. s.l. : Clarendon Press, Oxford, 1975.

59. **Von Dreele, R.B.** Neutron Powder Diffraction. [book auth.] D.L. Bish and Post J.E. *Modern Powder Diffraction.* Chelsea : BookCrafters, Inc., 1989.

60. About Us. *Oak Ridge National Laboratory-Neutron Sciences.* [Online] [Cited: December 23, 2012.] http://neutrons.ornl.gov/about/.

61. **Huq, A., et al.** 2011, Z. Kristallogr. Proc., Vol. 1, p. 127.

62. **Rodriguez-Carvajal, J.** 1993, Physica B., Vol. 192, p. 55.

63. **Krawczyk, J., et al.** s.l. : J. Alloys and Compounds, 1995, Vol. 219, p. 203.

64. **Seto, H., Noda, Y. and Yomada, Y.** s.l. : J. Phys. Soc. Jpn., 1990, Vol. 59, p. 965.

65. **Noheda, B., et al.** s.l. : Phys Rev. B., 2002, Vol. 66, p. 054104.

66. **Jacobson, D., et al.** A New Neutron Imaging Facility at BT-6 for the Non-Destructive Analysis of Working Fuel Cells. *NIST Center for Neutron Research.* [Online] [Cited: December 24, 2012.] http://www.ncnr.nist.gov/AnnualReport/FY2003_html/RH2/.

Publications/Awarded Proposals

R. Bergstrom Jr., M. Wuttig, J. Cullen, R. Briber, P. Zavalij, C. Dennis, O. Garlea, and M. Laver, *"Morphotropic Phase Boundaries in Ferromagnets: $Tb_{1-x}Dy_xFe_2$ Alloys,"* Physical Review Letters 111, 017203 (2013)

Y. Han, Y. Liu, P. Zavalij, L. Salamanca-Riba, E. Cantando, **R. Bergstrom Jr.**, L. Li, and M. Wuttig, *"Magnetoelectric Relaxation in Rhombohedral $LiNbO_3$-$CoFe_2O_4$,"* Applied Physics Letters 100, 262907 (2012)

APS General User Proposal GUP-28790, entitled "Structural Changes of Terfenol-D at the Symmetry 1 – Symmetry 2 Morphotropic Phase Boundary" awarded two days of beam time. (04/25/2012)

APS General User Proposal GUP-29729, entitled "Structural Changes of Terfenol-D at the Symmetry 1 – Symmetry 2 Morphotropic Phase Boundary" awarded one day of beam time. (04/25/2012)

SNS proposal IPTS-7279 "Magnetic Changes of Terfenol-D at the Symmetry 1 – Symmetry 2 Morphotropic Phase Boundary" awarded two days of beam time. (04/25/2012)